Topological phonon polariton enhanced radiative heat transfer in bichromatic nanoparticle arrays mimicking Aubry-André-Harper model

B. X. Wang and C. Y. Zhao*

Institute of Engineering Thermophysics, School of Mechanical Engineering,
Shanghai Jiao Tong University, Shanghai 200240, China
and MOE Key Laboratory for Power Machinery and Engineering, Shanghai Jiao Tong University, Shanghai 200240, China

Topological phonon polaritons (TPhPs) are promising optical modes relevant in long-range radiative heat transfer, information processing, and infrared sensing, whose topological protection is expected to enable their robust existence and transport. In this work we show that TPhPs can be supported in one-dimensional bichromatic silicon carbide nanoparticle (NP) chains, and demonstrate that they can considerably enhance radiative heat transfer for an array much longer than the wavelength of radiation. By introducing incommensurate or commensurate modulations on the interparticle distances, the NP chain can be regarded as an extension of the off-diagonal Aubry-André-Harper model. By calculating the eigenstate spectra with respect to the modulation phase that creates a synthetic dimension, we demonstrate that under this type of modulation the chain supports nontrivial topological modes localized over the boundaries since the present system inherits the topological property of two-dimensional integer quantum Hall systems. In this circumstance the gap-labeling theorem and corresponding Chern number can be used to characterize the features of band gaps and topological edge modes. Based on many-body radiative heat transfer theory for a set of dipoles, we theoretically show the presence of topological gaps and midgap TPhPs can substantially enhance radiative heat transfer for an array much longer than the wavelength of radiation. We show how the modulation phase that acts as the synthetic dimension can tailor the radiative heat transfer rate by inducing or annihilating topological modes. We also discuss the role of dissipation in the enhancement of radiative heat transfer. We further present a theoretical analysis based on eigenvalue decomposition to quantitatively reveal the role of TPhPs. These findings therefore provide a fascinating route for tailoring near-field radiative heat transfer based on the concept of topological physics.

I. INTRODUCTION

The discovery of topological phases of matter has led to plenty of research interests in novel topological quantum materials [1] and inspired fascinating analogies in photonic [2], atomic [3], acoustic [4], and mechanical [5] systems. The most unique feature of these topological systems is that they can support strongly localized and unidirectionally propagating edge or interface states which are largely immune against the presence of disorder and impurities, thanks to the topological protection. Topological protection means that the existence of these states is a global property regarding the topology of the entire band structure, which disappears only if the gap closes [6]. As one of the most promising analogies, topological photonic systems [7–9] not only provide a playground for observing topological modes directly and exploring novel physics that is not easily accessible in electronic systems like long-range interactions [10] and non-Hermitian topology [11], but also have promising applications in unidirectional waveguides [12], optical isolators [13,14], topological lasers [15–17] and topological sensors [18], and so on.

A seemingly separate research field is thermal radiation heat transfer. Recently, Biehs and coworkers [19–21] and

the authors [22,23] proposed the possibility that topological optical modes may play an important role in the control of thermal radiation, especially in tailoring near-field radiative heat transfer. In fact, topological photonic systems generally rely on the specific arrangements of different microscale and nanoscale elements, which naturally bear an intrinsic connection with typical systems regarding many-body radiative heat transfer [24–29], if a temperature gradient exists within them. The most typical case is nanoparticle (NP) arrays. For instance, Biehs and coworkers [19–21] recently investigated plasmonic InSb NP arrays that are specifically arranged to mimic the one-dimensional (1D) and two-dimensional (2D) Su-Schrieffer-Heeger (SSH) models as well as the quantum spin Hall (QSH) system in honeycomb lattices. They showed that in the topologically nontrivial phases, thermal near-field energy density is significantly enhanced at the edges and corners (if there are topological corner states), and the edge modes opened additional heat flux channels, which dominate the radiative heat transport.

In this work, we attempt to study the topological edge states and radiative heat transfer in a similar system with richer underlying physics, that is a bichromatic NP array mimicking the well-known Aubry-André-Harper (AAH) model [30–34]. This model is a 1D tight-binding lattice model with onsite or/and hopping terms being cosine modulated. When this cosine modulation is incommensurate (commensurate)

*changying.zhao@sjtu.edu.cn

with the lattice, this system becomes quasiperiodic (periodic). In this manner, this type of lattice model is sometimes dubbed "bichromatic" [35]. The presence of cosine modulation gives rise to nontrivial topological properties that can be mapped to the 2D integer quantum Hall (IQH) system (namely, the well-known Harper-Hofstadter model in a square lattice with a perpendicular magnetic field), in the absence of a realistic magnetic field [2,30]. In this situation, the modulation phase ϕ appearing in the cosine function describing the modulation [cf. Eq. (1) below] plays the role of momentum (wave number) in a perpendicular synthetic dimension, which thus leads to an imaginary dimensional extension to 2D [30,31,36]. As a consequence, this model provides a playground for studying profound topological phase transitions and topological states in 1D.

Different from previous works regarding radiative heat transfer in topological many-particle systems regarding plasmonic NPs [19–21], our interest here is focused on the topological phonon polaritons (TPhPs) since they not only inherit the properties of deep-subwavelength confinement and low loss of phonon polaritons that are prominent for mediating significant near-field radiative heat transfer [37–44], but also exhibit topological protection and strong localization over the edges [22]. These features render TPhPs promising in long-range radiative heat transfer, information processing, and infrared sensing, in which topological protection is expected to enable their robust existence and transport.

In this work, we show that TPhPs can be supported in 1D bichromatic silicon carbide nanoparticle chains by introducing incommensurate or commensurate modulations on the interparticle distances, as an extension of the off-diagonal AAH model. We calculate the band structures (eigenstate spectra) with respect to the modulation phase ϕ, which plays the role of a synthetic dimension. We find the evidence showing the present system inherits the topological properties of 2D IQH systems, and the spectral position and number of these topologically protected edge modes are governed by the gap-labeling theorem, which dictates the topological invariant, i.e., the Chern number, indicating the validity of bulk-boundary correspondence. Based on many-body radiative heat transfer theory for a set of dipoles, we theoretically show the presence of topological gaps and midgap phonon polariton edge modes can considerably enhance radiative heat transfer, for an array much longer than the wavelength of thermal radiation. We show how the modulation phase that acts as the synthetic dimension can tailor the radiative heat transfer rate by inducing or annihilating topological modes. We also discuss the role of dissipation of the SiC material. A theoretical analysis based on eigenvalue decomposition then follows to quantitatively examine the role of TPhPs. These findings therefore provide a fascinating route for tailoring near-field radiative heat transfer based on the concept of topological physics.

II. MODEL

Consider a 1D array composed of spherical α-SiC (hexagonal) NPs aligned along the x axis. To mimic the AAH model, we introduce artificial modulations over the spacings between

adjacent NPs, given by [34,45]

$$x_{n+1} - x_n = d[1 + \eta \cos(2\pi \beta n + \phi)], \quad (1)$$

where x_n denotes the position of the nth NP, d introduces the on-average interparticle distance (or the periodic lattice constant before modulation), η determines the amplitude of the distance modulation, β is the periodicity of the modulation that controls the bichromaticity of the lattice. If it is irrational, we say the modulation is incommensurate while if it is rational the modulation is then commensurate. By cosine modulating the interparticle distance, the "hopping amplitudes" of photons between adjacent NPs are also cosine modulated due to the distance-dependent dipole-dipole interactions between NPs [cf. Eqs. (5) and (6) below], thus mimicking the conventional off-diagonal AAH model (i.e., modulations over the intersite hopping amplitudes for electrons). Moreover, the modulation phase ϕ is introduced to further modulate the positions of the NPs, and it can be regarded as the momentum (wave number) in a synthetic orthogonal dimension [30–34], as aforementioned. A detailed mapping from 1D off-diagonal AAH model to the 2D Harper-Hofstadter model can be found in the work by Kraus et al. [30]. As a result, the 1D chain can inherit the rich topological property of 2D IQH systems.

For clarity, in Fig. 1, we plot the interparticle distance $\Delta x_n = x_{n+1} - x_n$ as a function of particle number n, for incommensurate and commensurate lattices. System parameters are chosen as $d = 0.6$ μm and $\eta = 0.3$. In Fig. 1(a) for $\beta = (\sqrt{5} - 1)/2$, it is seen that the distribution of particle positions is clearly aperiodic or, more specifically, quasiperiodic. Quasiperiodic system is the intermediate phase with long-range order between periodic and fully disordered (random) systems, thus harboring a qualitatively different spectrum [46], as will be seen below. We can also realize the vital role of ϕ in modulating the positions of the NPs. In Fig. 1(b) for $\beta = \frac{1}{4}$, it can be observed that the chain becomes periodic, with a periodicity of four NPs in a unit cell, and the modulation functionality of ϕ is also evident.

A. Electric dipole approximation and coupled-dipole model

Since SiC NPs support strongly localized phonon polariton resonances in the infrared region around 11 μm due to excitation of transverse optical phonons, the permittivity of SiC can be described by a Lorentz model as [47]

$$\varepsilon_p(\omega) = \varepsilon_\infty \left(1 + \frac{\omega_L^2 - \omega_T^2}{\omega_T^2 - \omega^2 - i\omega\gamma} \right), \quad (2)$$

in which ω is the angular frequency of the driving field in the unit of cm^{-1} (wave number), $\varepsilon_\infty = 6.7$ is the high-frequency limit of permittivity, $\omega_T = 790$ cm^{-1} is the angular frequency of transverse optical phonons, $\omega_L = 966$ cm^{-1} is the angular frequency of longitudinal optical phonons, and $\gamma = 5$ cm^{-1} is the nonradiative damping coefficient [47]. Without loss of generality, the radius of the spherical SiC NP is fixed as $a = 0.1$ μm. Such a small NP (much smaller than the resonance wavelength of localized phonon polaritons) can be approximated as an electric dipole [22] (see Appendix E). In this situation the electromagnetic response of an individual SiC NP can be described by the dipole polarizability within the so-called radiative correction to balance scattering and
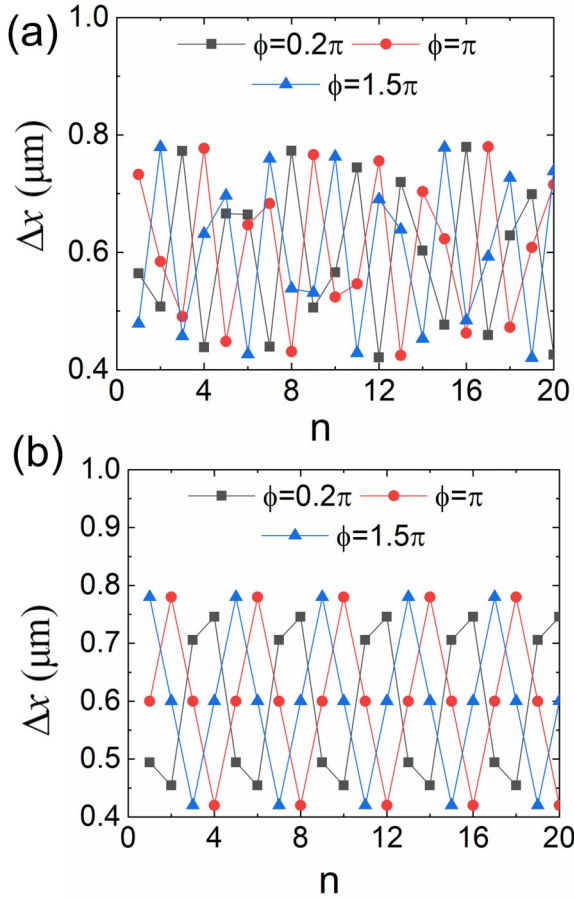
FIG. 1. The distribution of NP positions under different β and ϕ according to the generation rule of Eq. (1), described by the interparticle distance $\Delta x_n = x_{n+1} - x_n$. Only first 20 NPs are shown for clarity. (a) The incommensurate case $\beta = (\sqrt{5} - 1)/2$. (b) The commensurate case $\beta = \frac{1}{4}$. Other parameters are $d = 0.6$ μm and $\eta = 0.3$.

extinction [48–50]:

$$\alpha(\omega) = \frac{4\pi a^3 \alpha_0(\omega)}{1 - 2i\alpha_0(\omega)(k_0 a)^3/3} \tag{3}$$

with $k_0 = \omega/c$ being the free-space wave number and

$$\alpha_0(\omega) = \frac{\varepsilon_p(\omega) - 1}{\varepsilon_p(\omega) + 2}. \tag{4}$$

When the distance between the centers of adjacent spherical NPs is larger than $3a$ [by Eq. (1), the smallest interparticle distance is $d(1 - \eta) = 0.7d > 3a$ for $\eta = 0.3$], the electromagnetic (EM) response of the entire array is described by the well-known set of coupled-dipole equations [48–50]:

$$\mathbf{p}_j(\omega) = \alpha(\omega)\left[\mathbf{E}_{\text{inc}}(\omega, \mathbf{r}_j) + \frac{\omega^2}{c^2} \sum_{i=1, i\neq j}^{N} \mathbf{G}_0(\omega, \mathbf{r}_j, \mathbf{r}_i)\mathbf{p}_i(\omega) \right] \tag{5}$$

for $j = 1, 2, \ldots, N$, where c is the speed of light in vacuum. $\mathbf{E}_{\text{inc}}(\mathbf{r})$ is the external incident field (if any) and $\mathbf{p}_j(\omega)$ is the excited electric dipole moment of the jth NP. $\mathbf{G}_0(\omega, \mathbf{r}_j, \mathbf{r}_i)$ is

the free-space dyadic Green's function describing the propagation of field emitting from the ith NP to jth NP, which is given by [49]

$$\mathbf{G}_0(\omega, \mathbf{r}_i, \mathbf{r}_j) = \frac{\exp(ik_0 r)}{4\pi r}\left[\left(\frac{i}{k_0 r} - \frac{1}{k_0^2 r^2} + 1 \right)\mathbf{I} \right.$$
$$\left. + \left(-\frac{3i}{k_0 r} + \frac{3}{k_0^2 r^2} - 1 \right)\hat{\mathbf{r}}\hat{\mathbf{r}} \right], \tag{6}$$

with $r = |\mathbf{r}| = |\mathbf{r}_i - \mathbf{r}_j| > 0$ the distance between two NPs, and $\hat{\mathbf{r}}$ being the unit vector with respect to $\mathbf{r}$. Note the present model takes all types of near-field and far-field dipole-dipole interactions into account and is thus beyond the traditional nearest-neighbor approximation implemented in the conventional AAH model for electrons.

For 1D arrays, there are two types of electromagnetic modes, including the transverse and longitudinal ones [51]. For the longitudinal modes, the dipole moments of the NPs are aligned to the x axis, and therefore only the xx component of the Green's function (GF) needs to be used in calculations:

$$G_{0,xx}(x) = -2\left[\frac{i}{k_0|x|} - \frac{1}{(k_0|x|)^2} \right]\frac{\exp(ik_0|x|)}{4\pi|x|}. \tag{7}$$

On the other hand, for transverse eigenstates whose dipole moments are perpendicular to the array axis, the transverse (yy or zz) component of the GF is then used:

$$G_{0,yy}(x) = \left[\frac{i}{k_0|x|} - \frac{1}{(k_0|x|)^2} + 1 \right]\frac{\exp(ik_0|x|)}{4\pi|x|}. \tag{8}$$

To determine the band structure (eigenstate distribution) of a finite NP array, we can set the incident field in Eq. (5) to be zero [51,52]. Then an eigenvalue equation can be obtained:

$$\mathbf{M}|\mathbf{p}\rangle = \alpha^{-1}(\omega)|\mathbf{p}\rangle. \tag{9}$$

Here $\mathbf{M}$ stands for the interaction matrix whose elements are derived from the GF [Eqs. (7) and (8) according to the polarization of eigenmodes], for instance, for longitudinal modes, $M_{ij} = (\omega^2/c^2)G_{0,xx}(x_i - x_j)$ for $i \neq j$ and $M_{jj} = 0$. The right eigenvector of this equation $|\mathbf{p}\rangle = [p_1 p_2 \ldots p_j \ldots p_N]$, in the braket notation, stands for the dipole moment distribution of an eigenstate, where p_j is the dipole moment of the jth NP. This equation can be solved to get a series of complex eigenfrequencies in the lower complex plane in the form of $\tilde{\omega} = \omega - i\Gamma/2$, where the real part ω amounts to the angular frequency of the eigenstate while the imaginary part Γ corresponds to its linewidth (or decay rate of the eigenstate) [52,53].

Since the topologically protected eigenstates are highly localized over the boundary of the finite chain [3], to recognize these eigenstates clearly, we use the inverse participation ratio (IPR) to quantitatively measure for the localization degree of an eigenstate [54–57]:

$$\text{IPR} = \frac{\sum_{j=1}^{N} |p_j|^4}{\left(\sum_{j=1}^{N} |p_j|^2 \right)^2}. \tag{10}$$

An eigenstate with IPR $= 1$ is completely localized while an IPR $= 1/n$, where n is an integer, indicates the eigenstate can be regarded as evenly distributed over n NPs [54]. Therefore, for a highly localized topological edge state, its IPR should

be much larger compared to those of the bulk eigenstates [54]. But we should note not all eigenstates with high IPRs are topologically protected. For instance, Anderson localized states in the bulk are topologically trivial.

B. Calculation of radiative heat flux

Within the dipole approximation, the radiative heat transfer can be calculated semianalytically by employing the fluctuation-dissipation theorem (FDT). Radiative heat transfer in such a system is the simplest case of many-body radiative heat transfer, which has been discussed extensively in recent works [24–29]. Let us start from the coupled dipole model with fluctuating dipoles due to thermal excitation, which is [24]

$$\mathbf{E}_{ij} = \mu_0 \omega^2 \mathbf{G}_0^{ij} \mathbf{p}_{j \neq i}^{\text{fluc}} + \frac{\omega^2}{c^2} \sum_{k \neq i}^{N} \mathbf{G}_0^{ik} \alpha_k \mathbf{E}_{kj}, \tag{11}$$

in which $\mathbf{G}_0^{ij} \equiv \mathbf{G}_0(\omega, \mathbf{r}_i, \mathbf{r}_j)$ for brevity, $\mathbf{E}_{ij}$ is the exciting electric field impinging at particle i generated by the thermally induced fluctuating dipole moment of particle j, and α_k is the dipole polarizability of the kth particle, which is equal to α for identical NPs investigated in this work. The first term in the right-hand side is the direct propagation of a dipole field from the source $\mathbf{p}_{j \neq i}^{\text{fluc}}$, while the second summation term indicates the scattering processes from other particles k to particle i due to the exciting electric fields $\mathbf{E}_{kj}$ impinging on them. If we consider the total GF $\mathbf{G}^{ij}$ for the propagation of electromagnetic waves from the fluctuating dipole j with inclusion of the many-body scattering processes, which satisfies

$$\mathbf{E}_{ij} = \mu_0 \omega^2 \mathbf{G}^{ij} \mathbf{p}_{j \neq i}^{\text{fluc}}. \tag{12}$$

It can be directly solved from Eq. (11). Such total GF can be obtained for all particles with fluctuating dipoles. In a matrix notation, the total GF is given as [24]

$$\begin{pmatrix} \mathbf{G}^{1k} \\ \vdots \\ \mathbf{G}^{Nk} \end{pmatrix} = [\mathbf{I} - \mathbf{A}_0]^{-1} \begin{pmatrix} \mathbf{G}_0^{1k} \\ \vdots \\ \mathbf{G}_0^{(k-1)k} \\ 0 \\ \mathbf{G}_0^{(k+1)k} \\ \vdots \\ \mathbf{G}_0^{Nk} \end{pmatrix} \tag{13}$$

for $k = 1, \ldots, N$ with

$$\mathbf{A}_0 = \frac{\alpha(\omega) \omega^2}{c^2} \begin{pmatrix} 0 & \mathbf{G}_0^{12} & \cdots & \mathbf{G}_0^{1N} \\ \mathbf{G}_0^{21} & \ddots & \ddots & \vdots \\ \vdots & \ddots & \ddots & \mathbf{G}_0^{(N-1)N} \\ \mathbf{G}_0^{N1} & \cdots & \mathbf{G}_0^{N(N-1)} & 0 \end{pmatrix}. \tag{14}$$

Then by invoking FDT, the heat transfer rate from particle j to i is given by

$$\mathcal{P}_{j \to i} = 3 \int_0^\infty \frac{d\omega}{2\pi} \Theta(\omega, T_j) \mathcal{T}_{i,j}(\omega) \tag{15}$$

in which $\Theta(\omega, T) = \hbar \omega / \{\exp[\hbar \omega / (k_b T)] - 1\}$ is the Planck oscillator with $\hbar$ and k_b being the reduced Planck and Boltzmann constants respectively, and the transmission coefficient

(TC) is defined as

$$\mathcal{T}_{i,j}(\omega) = \frac{4}{3} \frac{\omega^4}{c^4} \chi_i \chi_j \text{Tr}[\mathbf{G}^{ij} \mathbf{G}^{ij\dagger}], \tag{16}$$

where $\chi_i = \text{Im}(\alpha_i) - k_0^3 |\alpha|^2 / (6\pi)$. A detailed derivation and description of above formulas is given in Refs. [24,28].

III. INCOMMENSURATE LATTICE

As mentioned, if β is irrational, we say the modulation is incommensurate and the NP array becomes quasiperiodic. Here, we consider the case of $\beta = (\sqrt{5} - 1)/2$, which is most commonly investigated incommensurate AAH lattice in previous works. We can plot the calculated eigenstate spectrum (band structure) as a function of ϕ, which varies in the range from 0 to 2π. We emphasize that the so-called band structure is nothing but a sweeping collection of eigenstate distributions of individual 1D chains generated by different ϕ's. Note it is not a band structure of 2D arrays of NPs and no mutual interactions take place between different chains, as ϕ only represents an imaginary dimension [31,58]. In Fig. 2(a), the longitudinal band structure of a chain with $N = 100$ NPs and $d = 0.6$ μm is shown, in which the color of eigenstates stands for their IPRs. The modulation amplitude is chosen to be a moderate value of $\eta = 0.3$, which does not affect the generality of this work [58] (a discussion on the effect of a larger η is given in Appendix D). It can be observed that the band structures break into a set of bands, in which large main gaps can be clearly seen with several discernible minigaps as well as many indiscernible gaps, that can be only seen in an enlarged figure (not shown here) [58]. This is due to the irrational nature of the interparticle distance modulation that leads to a fractal spectrum. In fact, for an infinitely long chain, its spectrum constitutes a Cantor set with Lebesgue measure zero [59–62]. This is a typical feature of quasiperiodic systems. Moreover, all the bands are actually flat and the eigenfrequencies are almost unchanged with the variation of ϕ with a few states crossing the gaps since the irrational modulation makes the system insensitive to lattice translation [31].

In the two main gaps, namely, the gaps covering 927.7 cm^{-1} $\lesssim \omega \lesssim$ 928.5 cm^{-1} and 928.6 cm^{-1} $\lesssim \omega \lesssim$ 929.3 cm^{-1} in Fig. 2(a), midgap states with high IPRs can be clearly recognized. These states are topologically protected edge states dictated by a nonzero Chern number, similar to the behavior of the conventional AAH model, as will be discussed below. These midgap states only exist for a specific range of modulation phase ϕ's. To see this more clearly, let us consider the eigenstate spectra of two cases, $\phi = 0.2\pi$ [Fig. 2(b)] and $\phi = \pi$ [Fig. 2(c)]. The state number is assigned according to its frequency. In the former case, no midgap states can be found, where the high-IPR eigenstates are actually bulk states that are Anderson localized [58] (not shown here). Note Anderson localization is due to the constructive interference between multiple scattering trajectories, which can emerge in disordered systems, and also can appear in certain quasiperiodic systems like the current system mimicking the AAH model, when the quasiperiodic modulation amplitude exceeds a certain value [63]. In the case of $\phi = \pi$ [Fig. 2(c)], in each of the two main gaps, a pair of midgap states are
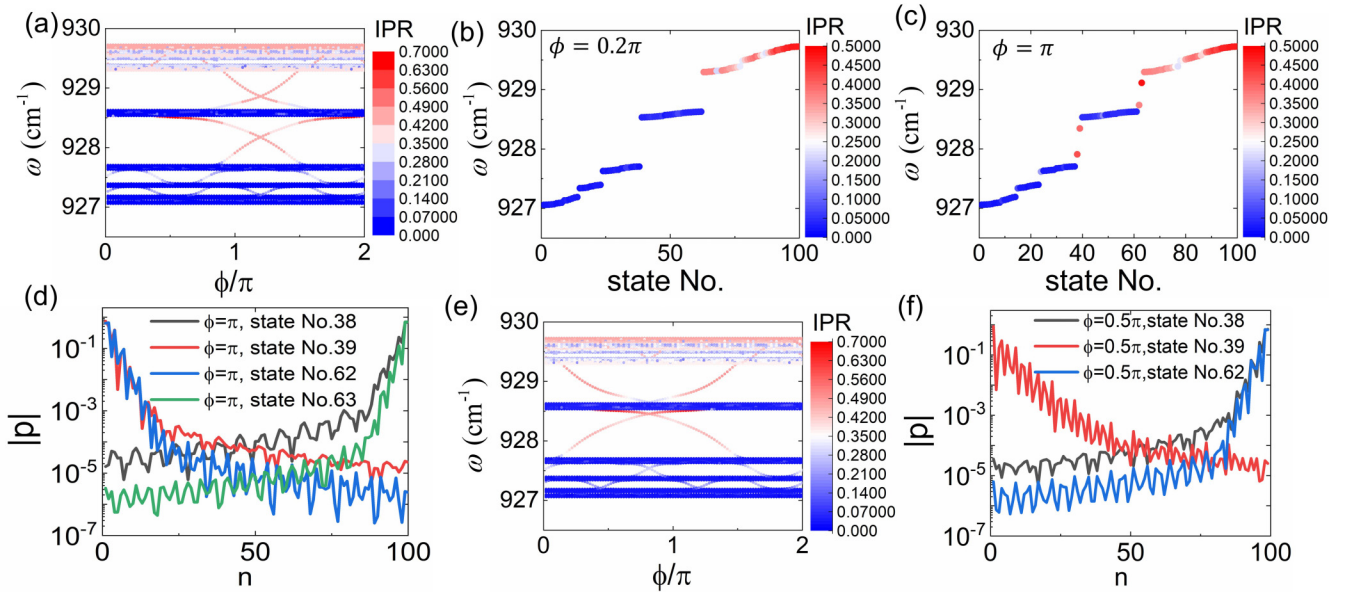
FIG. 2. Longitudinal band structures of incommensurate lattices with $\beta = (\sqrt{5} - 1)/2$, $d = 0.6$ μm, $\eta = 0.3$, and $N = 100$. (a) Band structure with respect to the modulation phase ϕ. (b) Eigenstate spectrum for $\phi = 0.2\pi$. (c) Eigenstate spectrum for $\phi = \pi$. (d) Dipole moment distributions of several typical midgap states. (e) Band structure for an array with an odd number of NPs ($N = 99$) as a function of modulation phase ϕ. (f) Dipole moment distributions for the midgap states for $\phi = 0.5\pi$.
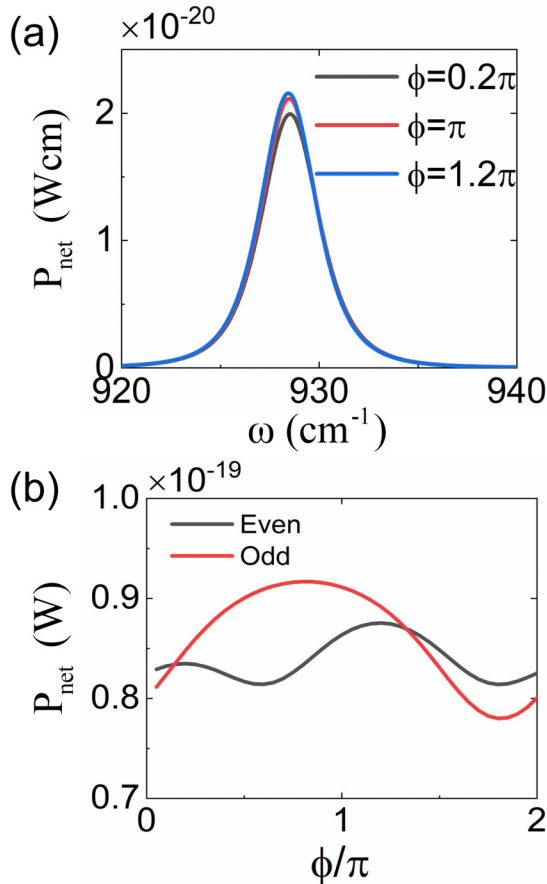

FIG. 3. Radiative heat transfer in the incommensurate lattice of $\beta = (\sqrt{5} - 1)/2$. (a) Spectral net heat transfer rate for $\phi = 0.2\pi, \pi$, and 1.2π for the even chain ($N = 100$). (b) Total net radiative heat rate as a function of modulation phase ϕ for both even and odd cases.

observed. The state numbers are denoted by 38, 39, 62, and 63, respectively. The dipole moment distributions over the chain for these states are given in Fig. 2(d), showing they are strongly localized over the boundaries, as a manifestation of topological edge states. In each of the main gaps, the pair of midgap states are localized over the left and right edges, respectively. We further find that in each of the two main gaps, by varying the modulation phase ϕ, the midgap edge states keep localized over the same edge as long as they remain in the gap. Therefore, these midgap states localized over the same edge in the same band gap can be regarded as belonging to the same "mode" as ϕ plays the role of momentum in an extended dimension. For each of the two main gaps, there are two edge modes traversing the spectral gap, one localized over the left edge and the other localized over the right edge. This property is a manifestation of the topological nature of the band gaps [31].

The topological property of the conventional AAH model can be characterized by the gap Chern number ν, which satisfies the following Diophantine-type equation [64–67]:

$$\mathcal{N} = \mu + \nu\beta, \tag{17}$$

in which μ is an integer and $\mathcal{N}$ is the normalized integrated density of states (IDOS) in the gap. This equation is a general result derived from the magnetic translational symmetry in an IQH system with 2D Bloch electrons subjected to rational (hence described by a rational $\beta = p/q$ with p, q denoting two coprime integers) magnetic fields. By taking the irrational limit for β, it can also be applied to incommensurate systems [66,68,69]. This is the reason why the above equation can be still thought of as a Diophantine equation [30,69,70]. More details on the origin of this equation are introduced in Appendix A as well as in Refs. [46,58,69,71–73]. This equation has only one set of solutions (μ, ν) for an irrational
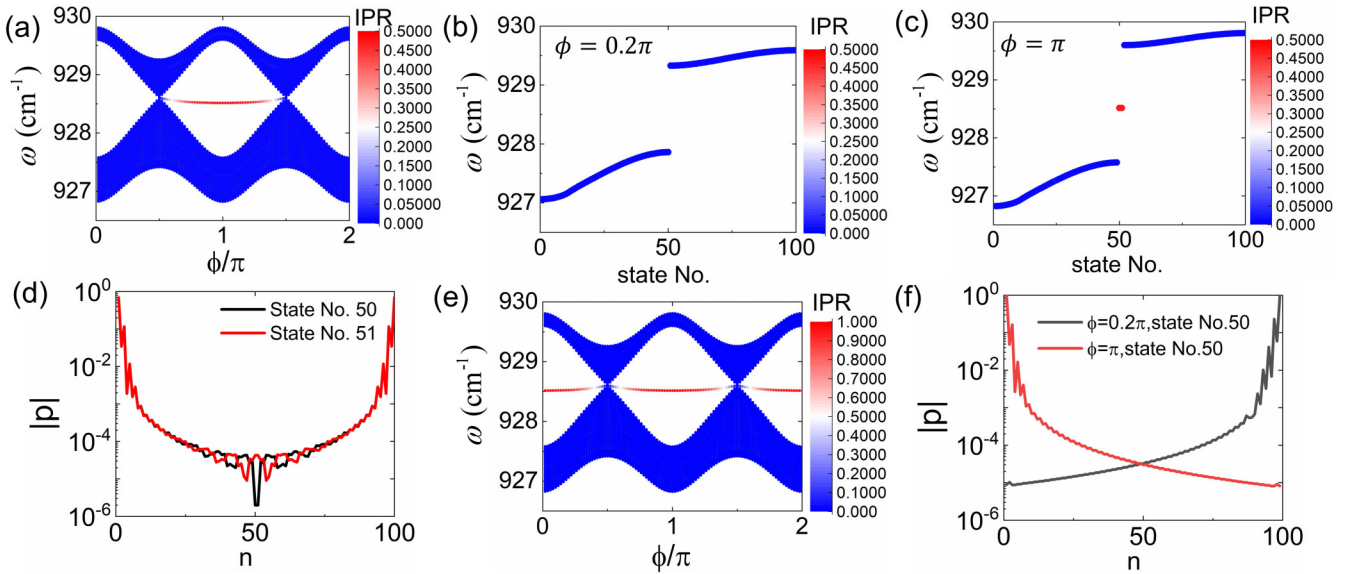
FIG. 4. Longitudinal band structures and midgap modes in the case of $\beta = \frac{1}{2}$, $N = 100$, $d = 0.6$ μm, and $\eta = 0.3$. (a) Band structure as a function of modulation phase ϕ. (b) Eigenstate distribution for $\phi = 0.2\pi$. (c) Eigenstate distribution for $\phi = \pi$. (d) Dipole moment distribution for the midgap states at $\phi = \pi$. (e) Band structure for an array with an odd number of NPs ($N = 99$) as a function of modulation phase ϕ. (f) Dipole moment distributions for the midgap states at $\phi = 0.2\pi$ and π in the odd case.

β and a fixed $\mathcal{N}$, and therefore any band gaps with the same $\mathcal{N}$ and irrational β can be labeled by the same set of integers (μ, ν), independent of system details. As a consequence, this equation is called the gap-labeling theorem [46,58,69,71–73]. This universality of these topological integers under an irrational β is robustly protected by the magnetic translational symmetry [70]. On the other hand, the situation is quite different for rational β's, where there are infinite solutions for the equation and therefore the topological property is system dependent [64,65,67,74].

To use the gap-labeling theorem, the normalized IDOS $\mathcal{N}$ of a band gap can be calculated, which is the number of eigenstates below the gap divided by the total number of eigenstates in the spectrum for a specific ϕ. In Fig. 2(a), the lower main gap (927.7 cm^{-1} ≲ ω ≲ 928.5 cm^{-1}) has an IDOS of $\mathcal{N} \approx$ 38/100 = 0.38, which leads to a solution for the gap-labeling theorem of $\mu = 1$, $\nu = -1$. It should be noted in a rigorous sense, for our case, the values of μ and ν are approximate because N is a rational number for our finite chain while β is an irrational number. When the length of the chain goes to infinite, the results of μ and ν become exact [54,71,72,75–85]. The upper main gap 928.6 cm^{-1} ≲ ω ≲ 929.3 cm^{-1} exhibits an IDOS $\mathcal{N} \approx$ 62/100 = 0.62, resulting in an integer solution of $\mu = 0$, $\nu = 1$. Therefore, the Chern number of the lower (upper) main gap, as a global property from the bulk band structure, is $\nu = -1$ ($\nu = +1$). According to the bulk-boundary correspondence in 2D IQHE, for a gap Chern number of ν, there must be $|\nu|$ edge mode(s) on each edge, whose energy (frequency) traverses the gap when ϕ varies from 0 to 2π [30,31,34]. The sign of gap Chern number determines the chirality (group velocity) of the left edge modes [34]. According to the observed topological edge modes in Figs. 2(b)–2(d), we can confirm that the bulk-boundary correspondence is valid in our system, and therefore the midgap

edge states are indeed topologically protected. In other words, they can be regarded as topological phonon polaritons.

We can further validate the bulk-boundary correspondence by investigating the minigaps with more midgap states, for instance, the minigap covering ω, which has an IDOS of 0.24 and a Chern number of $\nu = 2$, leading to two edge modes on both left and right edges (i.e., four edge modes in total), respectively. Since these midgap edge states in the minigaps will not contribute significantly to radiative heat transfer, we will not study them in detail [58]. Moreover, for the transverse eigenstates, the band gaps are substantially narrower as a consequence of weaker dipole-dipole interactions. This is because transverse eigenstates involve a far-field interaction term that decays very slowly with the distance r as $1/r$ [Eq. (8)]. Such far-field interactions can result in very long-range hoppings of excited states and effectively reduce the strength of near-field interactions, leading to a reduction in the band-gap width. In spite of these differences, the qualitative behavior is still quite similar to the conventional AAH model. Therefore, they will not be discussed in detail in this work. One can find related discussions in Refs. [19,55,58].

It is worth mentioning that the dipole moment distribution of the topological edge state shows a fast decay near the edge and then a slower one in the bulk [Fig. 2(d)]. More precisely, the topological edge states decay exponentially from the boundary with a relatively short localization length while decaying in power law in the long range, deep in the bulk. This feature is a consequence of algebraically (or power-law) decaying ($1/r^\alpha$, $\alpha > 0$) dipole-dipole interactions that give rise to long-range hopping of photons, which is also observed in many similar systems with power-law interactions, for instance, the 1D Kitaev model with power-law pairing [86] and 1D Kitaev model with both power-law hopping and pairing

[87,88]. A more evident demonstration has also been given in our previous work for a long chain with 2000 NPs [55].

For the AAH chain, there is a well-known even-odd effect with respect to the number of lattice sites. In Fig. 2(e), the band structure for an $N = 99$ lattice is given, where we can see one of the topological edge modes in the main gap does not change compared to the even case while the other is largely shifted in ϕ [89]. We can confirm it still fulfills the gap-labeling theorem and the dipole moment distributions of topological edge states are presented in Fig. 2(f).

Now let us consider how TPhPs affect radiative heat transfer in such a system. We assume the first NP has a temperature of $T_1 = 310$ K while all of the other NPs' temperatures are kept as $T_j = 300$ K, $j = 2, 3, \ldots, N$. This choice of temperature distribution is to partially match the resonance frequency of phonon polaritons in SiC. The net spectral heat rate from the first NP to the last NP, $P_{\mathrm{net}}^{N1}(\omega) = \mathcal{P}_{1 \to N, \omega} - \mathcal{P}_{N \to 1, \omega}$ for $\phi = 0.2\pi, \pi$, and 1.2π, is plotted in Fig. 3(a). Note the results take the contributions of both longitudinal and transverse polarizations into account, although we only investigate the longitudinal eigenstate spectra. It is found that there are considerable differences between the maximum spectral radiative heat rate $P_{\mathrm{net,max}}^{N1}$ in these three cases. For $\phi = 0.2\pi$, since there is not any TPhP [Figs. 2(a) and 2(b)], $P_{\mathrm{net,max}}^{N1}$ is the smallest. In both cases of $\phi = \pi$ and 1.2π, TPhPs are present in the main gaps [Figs. 2(a), 2(c), and 2(d)], which enhance the radiative heat transfer process. Moreover, $P_{\mathrm{net,max}}^{N1}(\phi = 1.2\pi)$ is slightly larger than $P_{\mathrm{net,max}}^{N1}(\phi = \pi)$, because in the case of $\phi = 1.2\pi$, there are two nearly degenerate edge states below the central bands (also near the phonon polariton resonance frequency $\omega \sim 928.5$ cm^{-1} of a single NP) that can further enhance the long-range heat transfer (consider the length of the chain is around $\sim 100d = 60$ μm and refer to theoretical analysis in Sec. V).

In the odd case, one of the topological edge modes in the main gap does not change compared to the even case while the other is largely shifted in ϕ [Fig. 2(e)]. We also found that this shift of topological edge mode has a significant effect on radiative heat transfer. Figure 3(d) shows the total net radiative heat transfer rate (integrated over all frequencies) $P_{\mathrm{net}}^{N1} = \mathcal{P}_{1 \to N} - \mathcal{P}_{N \to 1}$ for the even and odd cases as a function of modulation phase ϕ, in which it is clearly seen that this variation closely resembles the evolution of topological edge modes with ϕ in both even and odd cases [Figs. 2(a) and 2(e)]. That is, the existence of TPhPs can significantly enhance P_{net}^{N1}, and if there are more topological edge states approaching the central band ($\omega \sim 928.5$ cm^{-1}, namely, near the phonon polariton resonance frequency of a single NP), the larger P_{net}^{N1} is. Since the shift of topological mode in the odd case leads to a major change of the ϕ dependence compared to the even case, we can further confirm that TPhPs play an important role in this long-range radiative heat transfer process.

IV. COMMENSURATE LATTICE

In this section we further discuss the cases of rational β's, namely, commensurate lattice. We will mainly focus on two cases: $\beta = \frac{1}{2}$ and $\frac{1}{4}$.
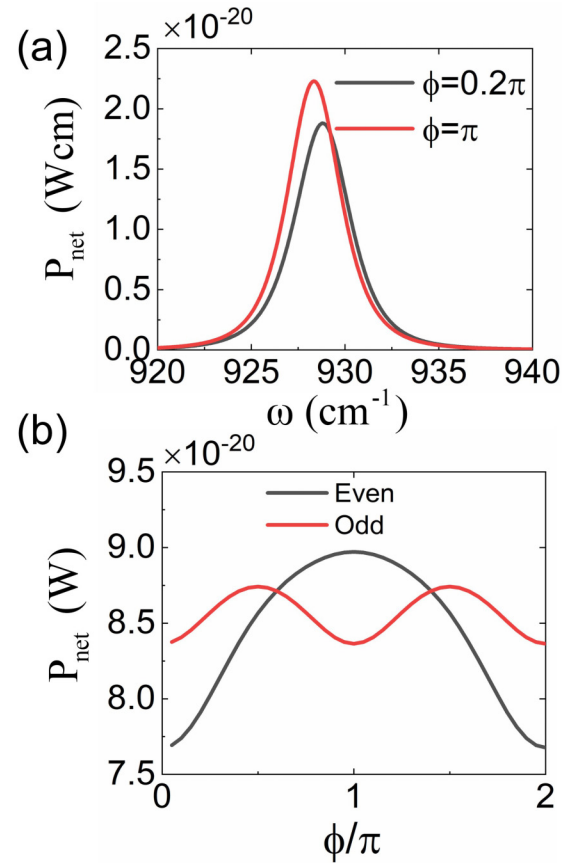

FIG. 5. Radiative heat transfer in the case of $\beta = \frac{1}{2}$. (a) Spectral net heat transfer rate for $\phi = 0.2\pi$ and π in the even case. (b) Total net radiative heat rate as a function of modulation phase ϕ for both even and odd cases.

A. The case of $\beta = \frac{1}{2}$

In Fig. 4(a), the eigenstate spectrum for $\beta = \frac{1}{2}$ is presented with $N = 100$, $d = 0.6$ μm, and $\eta = 0.3$. There is no band gap in the spectrum, with two degenerate points which can be regarded as Dirac points [32,90]. A quasi-zero-energy mode (that is near the resonance frequency of phonon polaritons) exists and connects the two Dirac points. All bulk eigenstates have low IPR values and are extended states. Unlike the situation of the conventional AAH model under nearest-neighbor (NN) approximations without long-range hoppings, the frequency of this quasi-zero-energy mode is not kept constant with ϕ but slightly changes [32,91,92]. We also note in the commensurate system, the band is no longer flat and varies substantially with ϕ since the translational invariance only exists for discrete values of ϕ ($\phi = \pi$ for $\beta = \frac{1}{2}$) [31]. Although the entire system as a family of 1D lattices does not have a full band gap, when a specific configuration with a fixed $\phi \neq 0.5\pi$ or π is considered, there is still a band gap, as shown in Fig. 4(b) for $\phi = 0.2\pi$ and Fig. 4(c) for $\phi = \pi$. As expected, there is no midgap state in the case of $\phi = 0.2\pi$ while two degenerate midgap states emerge in the band gap for the case of $\phi = \pi$, whose dipole moment distributions are given in Fig. 4(d). These midgap modes are indeed localized over the boundaries. As discussed in previous works for the off-diagonal AAH model with NN hoppings
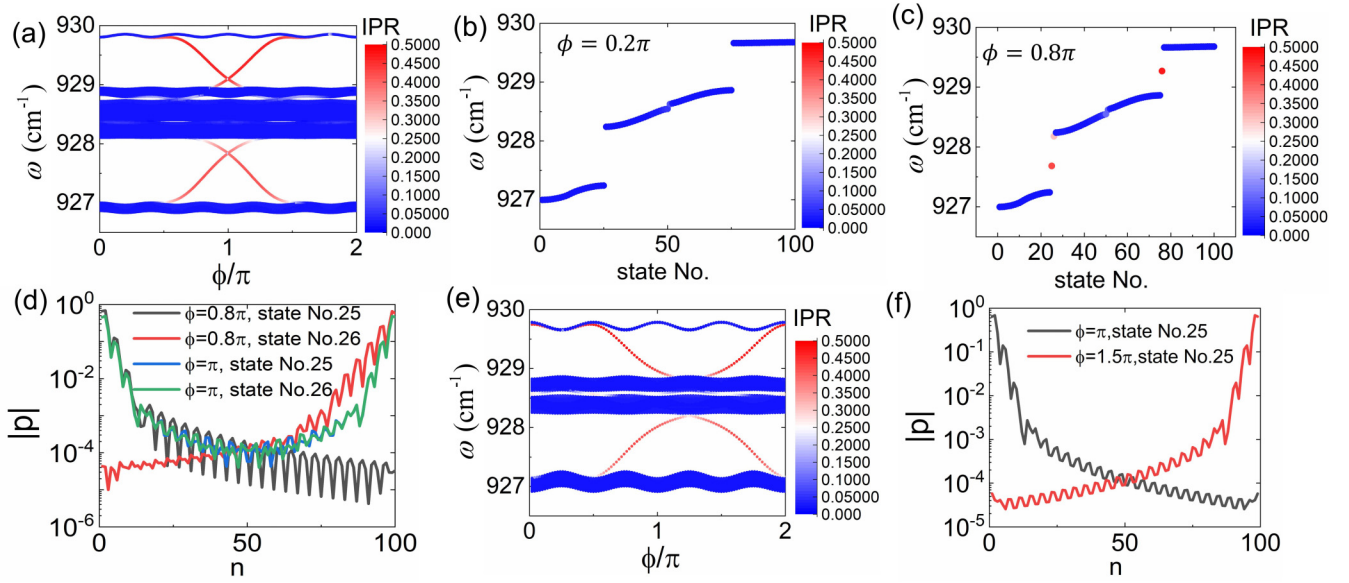
FIG. 6. Longitudinal band structures and midgap modes in the case of $\beta = \frac{1}{4}$, $N = 100$, $d = 0.6$ μm, and $\eta = 0.3$. (a) Band structure as a function of modulation phase ϕ. (b) Eigenstate distribution for $\phi = 0.2\pi$. (c) Eigenstate distribution for $\phi = 0.8\pi$. (d) Dipole moment distributions for the midgap states in the cases of $\phi = 0.8\pi$ and π. (e) Band structure for an array with an odd number of NPs ($N = 99$) as a function of modulation phase ϕ. (f) Dipole moment distributions for the midgap states for $\phi = 0.2\pi$ and π in the odd case.

under $\beta = \frac{1}{2}$ [32], the topology property for such a system, as a family of 1D systems, can be more conveniently understood in a Majorana basis, which can be described by a Z_2 topological index. This index is 0 for $\cos\phi > 0$ while it is 1 for $\cos\phi < 0$ in our system, consistent to the emergence of quasi-zero-energy modes. Note although there are long-range dipole-dipole interactions in the present system, they can be regarded as small perturbations which do not affect the robustness of topological edge modes as implied in Ref. [32] since the interparticle distance is deep subwavelength and the nearest-neighbor coupling dominates. On the other hand, for a specific ϕ, the band topology can be described by the Zak phase for 1D systems like the conventional SSH model with trivial chiral symmetry breaking due to next-nearest-neighbor (NNN) and high-order hoppings, which is well understood in previous works of the authors and others [22,52,93]. In the meanwhile, there is also an even-odd effect for $\beta = \frac{1}{2}$ as expected. Figure 4(e) shows the eigenstate spectrum for $N = 99$. It is found in this odd case, quasi-zero-energy mode exists for all ϕ's. However, we note these edge states only localize over one of the boundaries [Fig. 4(e)], different from the even case in which the edge states are localized over both boundaries (therefore with lower IPRs ∼0.5) [Fig. 4(c)]. As discussed in Ref. [32], in the Majorana basis, there always exists a single Majorana localized on one of the edge sites.

Let us proceed to the calculation of radiative heat transfer. The net spectral heat rate from the first NP to the last NP, $P_{net}^{N1}(\omega)$ for $\phi = 0.2\pi$ and π, is plotted in Fig. 5(a). A significant difference between the spectrum of the topological phase ($\phi = \pi$) and that of the topologically trivial case ($\phi = 0.2\pi$) is observed, in which the former shows a considerably larger maximum spectral radiative heat rate $P_{net,max}^{N1}$, indicating the enhancement of radiative heat transfer due to TPhPs. Moreover, the spectral position of this maximal value is different between topologically nontrivial and trivial cases. This is be-

cause for the former case, $P_{net,max}^{N1}$ comes from the excitation of TPhPs in the gap while in the latter case it is due to the transport enhancement originated from the band edges of bulk spectrum [18].

We compare the total net radiative heat transfer rate P_{net}^{N1} for the even and odd cases as a function of modulation phase ϕ in Fig. 5(b). In the even case, the variation is closely related to the evolution of topological edge modes with ϕ [Fig. 4(a)], where the maximum value is resided at $\phi = \pi$ with topological edge states with highest localization degree (i.e., IPR) while the topologically trivial regime shows the smallest heat rate. On the other hand, for the odd case, since topological edge states are present for all ϕ's [Fig. 4(e)], the amplitude of variation of P_{net}^{N1} with ϕ is small, and the maximum heat transfer rate emerges at the Dirac points. The on-average P_{net}^{N1} in the odd case is still large, comparable with the heat transfer rate in the topological phase in the even configuration, while it is considerably lower than the maximum P_{net}^{N1} in the even case. Note the length of the array in the odd case is shorter than that of the even case. This important difference derives from the fact that two-sided edge states can show a stronger augmentation of long-range energy transfer than one-side edge states, consistent with previous findings in Ref. [19], as would be also explained by our theoretical analysis in Sec. V below. Therefore, we can further confirm that the presence of TPhPs can indeed enhance long-range heat transfer significantly.

B. The case of $\beta = \frac{1}{4}$

We further investigate the case of $\beta = \frac{1}{4}$, whose eigenstate spectrum as a function of ϕ for a lattice with $N = 100$ NPs is shown in Fig. 6(a). Due to this periodic modulation, the band structure breaks into four bands, with two clearly visible main band gaps and one very small gap in the middle of the spectrum. For the conventional AAH model with only NN

coupling, there is no such a gap and the two middle bands are connected by four Dirac points [90]. The difference here is due to the NNN and high-order hoppings as discussed in detail in Ref. [32]. We also note in each of the main gaps, there are two midgap modes with high IPRs. These modes are also topologically protected edge modes. Like previous cases, these modes only exist for a specific range of ϕ. For instance, for the case of $\phi = 0.2\pi$ [Fig. 6(b)], there are three band gaps recognized, without any midgap states, while for $\phi = 0.8\pi$ [Fig. 6(c)], two midgap states in the lower main gap and one midgap state in the upper main gap are clearly observable. The dipole moment distributions of the two midgap states in the lower main gap (state numbers are 25 and 26) are shown in Fig. 6(d): They are localized over the left and right boundaries, respectively. Moreover, for $\phi = \pi$, the two midgap modes cross with each other and the two midgap states become nearly degenerate, and thus they are localized over both of the boundaries of the chain and almost overlap with each other.

In this case, the topological properties of the gaps are determined by the Chern number. As aforementioned, the gap-labeling theorem is still valid in the commensurate case but the solution is no longer unique like the incommensurate case. Therefore, Chern number for a band n here can only be directly computed by formally carrying out Berry curvature integration through the "ancestor" 2D quantum Hall model [34,91]:

$$\nu_n = \frac{1}{2\pi} \int_0^{2\pi} \int_0^{2\pi/(2d)} dk \, d\phi \left(\frac{\partial A_k}{\partial \phi} - \frac{\partial A_\phi}{\partial k} \right) \quad (18)$$

in a 2D parameter space with ϕ being the wave number in the extended dimension in addition to the wave number k in the real 1D space (since the 1D chain is periodic). Here $A_k = i\langle \psi_n(k) | \partial_k | \psi_n(k) \rangle$ and $A_\phi = i\langle \psi_n(k, \phi) | \partial_\phi | \psi_n(k, \phi) \rangle$ with ψ_n being the wave function in the band n, which can be solved by applying the Bloch theorem under periodic boundary condition and consists of the dipole moments of four NPs in a unit cell in our system. The gap Chern number is the sum of the band Chern numbers below the gap. It is found for the lower gap $\nu = -1$, while for the upper gap, $\nu = +1$. These Chern numbers guarantee the existence of $|\nu| = 1$ topological edge mode at both of the edges in both gaps. Hence, the edge modes emerging at the two main gaps are indeed topologically protected.

The even-odd effect is still persistent, demonstrated by the eigenstate spectrum for $N = 99$ shown in Fig. 6(e). It is seen that one of the topological edge modes significantly shifts along the ϕ coordinate. The dipole moment distributions of two eigenstates at $\phi = \pi$ and 1.5π are further presented in Fig. 6(f) to confirm they are topological edge states.

Figure 7(a) shows the net spectral heat rate from the first NP to the last NP, $P_{\text{net}}^{N1}(\omega)$ for $\phi = 0.2\pi$, 0.8π, and π in the even case. Like previous scenarios, considerable differences between the maximum spectral radiative heat rate $P_{\text{net,max}}^{N1}$ in these three cases are observed. $P_{\text{net,max}}^{N1}$ at $\phi = 0.2\pi$ is the smallest due to the absence of TPhPs [Figs. 6(a) and 6(b)], while in both situations of $\phi = 0.8\pi$ and π, the presence of TPhPs [Figs. 6(a) and 6(c)] can substantially enhance the heat transfer rate present in the main gaps. Like previous cases, $P_{\text{net,max}}^{N1}(\phi = \pi)$ is slightly larger than $P_{\text{net,max}}^{N1}(\phi = 0.8\pi)$,
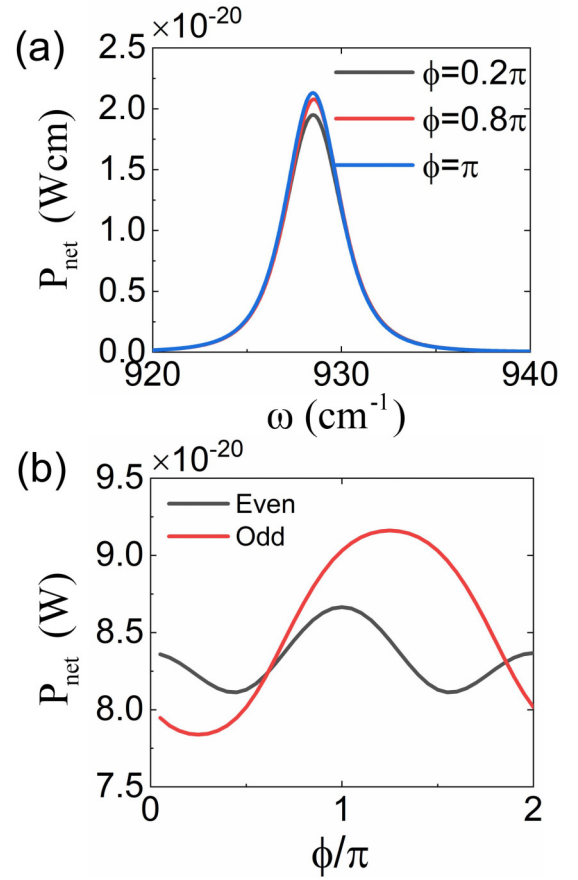
FIG. 7. Radiative heat transfer in the case of $\beta = \frac{1}{4}$. (a) Spectral net heat rate for $\phi = 0.2\pi$, 0.8π, and π in the even case. (b) Total net radiative heat rate as a function of modulation phase ϕ for both even and odd cases.

thanks to the existence of two nearly degenerate topological edge states near central band [Fig. 6(a)] that can further enhance the long-range heat transfer.

The shift of topological modes in the odd case, as expected, has a significant influence on the ϕ dependence of total heat transfer rate P_{net}^{N1} [Fig. 7(b)]. The general trend in both even and odd cases follows the evolution of topological edge modes like previous cases. As a result of two degenerate TPhPs approaching closely the central band, in the odd case (at $\phi \sim 1.2\pi$), it exhibits the largest total heat transfer rate.

We would like to discuss the role of dissipation of the SiC material in this study of TPhP enhanced radiative heat transfer. We assume a low-loss circumstance of $\gamma = 1 \text{ cm}^{-1}$ for the permittivity in Eq. (2) with other parameters unchanged. In this case, the eigenstate spectrum shows almost no difference with the case of $\gamma = 5 \text{ cm}^{-1}$ (not shown here). The net spectral heat transfer rate from the first NP to the last NP $P_{\text{net}}^{N1}(\omega)$ for $\phi = 0.2\pi$, 0.8π, and π is shown in Fig. 8(a). More significant differences between these spectra than previous high-loss cases are observed. On one hand, the topological phases ($\phi = 0.8\pi$ and π) show several times larger maximum spectral radiative heat rates $P_{\text{net,max}}^{N1}$ than the topologically trivial case ($\phi = 0.2\pi$), clearly confirming the enhancement of radiative heat transfer due to TPhPs. Moreover, the spectral position of this maximal value is different for the
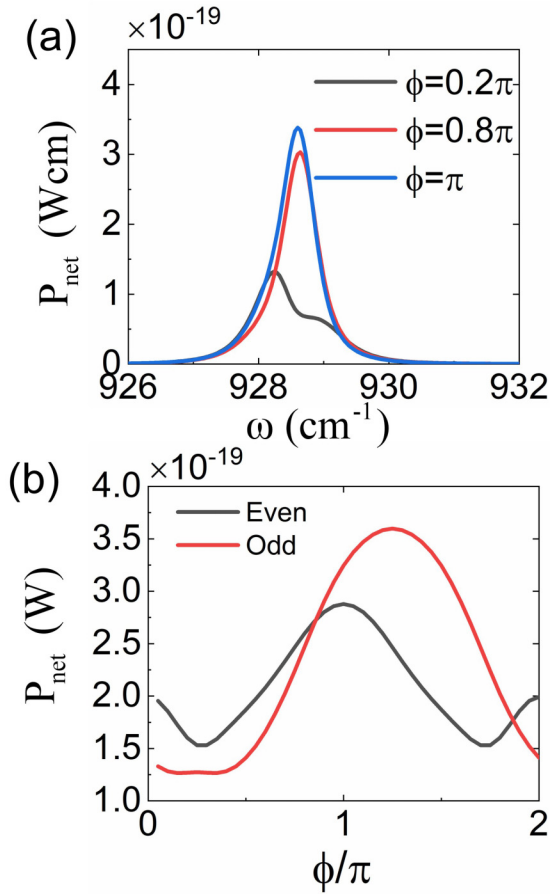
FIG. 8. Radiative heat rate in the case of $\beta = \frac{1}{4}$ with an artificial decay rate $\gamma = 1 \text{ cm}^{-1}$. (a) Spectral heat rate for $\phi = 0.2\pi$, 0.8π, and π for the even case. (b) Total radiative heat rate as a function of modulation phase ϕ for even ($N = 100$) and odd ($N = 99$) cases. Other parameters are $d = 0.6 \, \mu\text{m}$ and $\eta = 0.3$.

topologically nontrivial and trivial cases, similar to the reason of the difference in Fig. 5(a). That is, for the topologically nontrivial cases, $P_{\text{net,max}}^{N1}$ is dominated by the excitation of TPhPs in the gap while in the topologically trivial case it is due to the transport mediated by the eigenstates in bulk bands [18]. More specifically, for the topologically trivial case ($\phi = 0.2\pi$), two moderate peaks appear at around $\omega = 928.3$ and $928.8 \, \text{cm}^{-1}$, which essentially correspond to the eigenstates lying at the edges of central two bands. This is expected since eigenstates at band edges show large group velocities and then a large density of states (DOS). [Note, for periodic nanoparticle chains, state number is proportional to Bloch wave number of the state [51,52,55]. In particular, for kth eigenstate, the real part of elements in the eigenvector varies from positive to negative alternately along the chain, and the number of times the sign changes is $(k-1)$, from which the wave number can hence be determined.]

In Fig. 8(b), total radiative heat rate P_{net}^{N1} as a function of modulation phase ϕ for the even and odd lattices is provided, which unequivocally shows the giant enhancement brought by the existence of TPhPs. Notably in the odd case, the presence of TPhPs demonstrates nearly three times larger total radiative heat transfer rate P_{net}^{N1} than that of the topologically trivial

lattice. Therefore, the considerable damping coefficient in the SiC material is the critical factor that affects the enhancement brought by TPhPs [21]. We envision that future works to explore phonon polaritonic materials with lower losses will be critical to achieving a significant enhancement of the radiative heat transfer mediated by topological edge modes. These low-loss materials will also facilitate the experimental observation of TPhP-enhanced radiative heat transfer.

V. DISCUSSION

In this section, we aim to theoretically reveal why topological edge states can enhance radiative heat transfer. Without loss of generality, we consider only longitudinal modes as an illustration. In this manner, the matrix elements in Eq. (13), $\mathbf{G}_0^{ij}$ and $\mathbf{G}^{ij}$, become scalar. In this scenario, the $N \times N$ matrix $\mathbf{A}_0$ in Eq. (13) is related to the interaction matrix $\mathbf{M}$ in Eq. (9) as $\mathbf{A}_0 = \alpha \mathbf{M}$. We denote the eigenvalues of the matrix $\mathbf{M}$ as λ_k with corresponding eigenvectors $\mathbf{V}_k$, and then the matrix $\mathbf{M}$ can be diagonalized as

$$\mathbf{M} = \mathbf{VDV}^{-1}, \quad (19)$$

with $\mathbf{D} = \text{diag}(\lambda_1, \lambda_2, \ldots, \lambda_k, \ldots, \lambda_N)$ and $\mathbf{V} = [\mathbf{V}_1, \mathbf{V}_2, \ldots, \mathbf{V}_k, \ldots, \mathbf{V}_N]$. Note here each column vector $\mathbf{V}_k$ is the same as the dipole moment distribution $|\mathbf{p}\rangle = [p_1 p_2 \ldots p_j \ldots p_N]$ in Eq. (9). Thus, we get

$$\begin{pmatrix} \mathbf{G}^{1k} \\ \vdots \\ \mathbf{G}^{Nk} \end{pmatrix} = \mathbf{V}^{-1}[\mathbf{I} - \alpha\mathbf{D}]^{-1}\mathbf{V} \begin{pmatrix} \mathbf{G}_0^{1k} \\ \vdots \\ \mathbf{G}_0^{(k-1)k} \\ 0 \\ \mathbf{G}_0^{(k+1)k} \\ \vdots \\ \mathbf{G}_0^{Nk} \end{pmatrix}. \quad (20)$$

Since the matrix $\mathbf{M}$ is symmetric, we have $\mathbf{V}^{-1} = \mathbf{V}^{\text{T}}$. After some matrix manipulations, we obtain the elements of total GF as

$$G^{ij} = \sum_{k=1}^{N} \sum_{m=1}^{N} V_{k,i} \frac{1}{1 - \alpha(\omega)\lambda_k} V_{m,k} G_{0,xx}^{mj}, \quad m \neq j \quad (21)$$

in which $V_{k,i}$ is the ith element of the kth eigenvector $\mathbf{V}_k$, proportional to the dipole moment of the ith NP in this eigenstate, and $G_{0,xx}^{mj} = G_{0,xx}(x_j - x_m)$.

From Eq. (16), for the scalar case regarding longitudinal eigenstates we obtain the transmission coefficient as

$$\mathcal{T}_{i,j}(\omega) = \frac{4}{3} \frac{\omega^4}{c^4} \chi_i \chi_j \left| \sum_{k=1}^{N} \sum_{m=1, m \neq j}^{N} \frac{V_{k,i} V_{m,k}}{1 - \alpha(\omega)\lambda_k} G_{0,xx}^{mj} \right|^2. \quad (22)$$

For the TC between the NPs at the opposite ends, we get

$$\mathcal{T}_{N,1}(\omega) = \frac{4}{3} \frac{\omega^4}{c^4} \chi_N(\omega) \chi_1(\omega)$$

$$\times \sum_{k=1}^{N} \left| \frac{1}{1 - \alpha(\omega)\lambda_k} \right|^2 |V_{k,N}|^2 \left| \sum_{m=2}^{N} V_{k,m} G_{0,xx}^{m1} \right|^2. \quad (23)$$

Therefore, the TC can be decomposed into the contributions of all eigenstates. As a matter of fact, for a specific ω, those eigenstates with eigenfrequency ω_k lying in the range of $[\omega - \gamma/2, \omega + \gamma/2]$ would contribute most to the TC, while the contribution of other eigenstates is usually negligible. This is actually determined by the $|1/[1 - \alpha(\omega)\lambda_k]|^2$ prefactor in each term in the summation [19,49,55,94], as would be discussed later. This prefactor, to some extent, can be regarded as an indicator for density of states, as it determines how many eigenstates determine the response of the system at a specific frequency.

The significant contribution from topological edge states can be understood from Eq. (23). First, it is evident that the term $|V_{k,N}|^2$ in Eq. (23) would be much larger when kth eigenstate is a topological edge state localized over the Nth NP than when it is a bulk state. This was also implied by Ref. [19]. Second, we note the summation $|\sum_m V_{k,m} G_{0,xx}^{m1}|^2$, at the rightmost of Eq. (23), shows quite different behaviors for edge and bulk states. If the kth eigenstate is a bulk state, the real part of elements in the eigenvector $\mathbf{V}_k$ varies from positive to negative alternately along the chain, and the number of times the sign of $V_{k,m}$ changes is $(k-1)$ [51,52]. In this sense, the term $|\sum_m V_{k,m} G_{0,xx}^{m1}|^2$ in the rightmost of Eq. (23) is expected to be small due to the cancellation of positive and negative elements. On the other hand, if the kth eigenstate is a topological edge state which decays exponentially near the boundaries, the product $V_{k,m} G_{0,xx}^{m1}$ would be large near the boundaries and nearly zero in the bulk, resulting in relatively large values of $|\sum_m V_{k,m} G_{0,xx}^{m1}|^2$. Since the arrangement of NPs in our system is not simple, the eigenvectors of the interaction matrix cannot always be obtained analytically, especially for topological edge states. To verify above arguments, we thus numerically calculate the results of $|\sum_m V_{k,m} G_{0,xx}^{m1}|^2$ for bulk and topological edge states.

The results are shown in Fig. 9(a) for the incommensurate case $\beta = (\sqrt{5} - 1)/2$, and in Fig. 9(b) for the commensurate case $\beta = \frac{1}{4}$, respectively, in logarithmic scale. In the former case, three highest values are identified, with state numbers 24, 39, and 62, which correspond to topological edge states as aforementioned, while there are also two large values ($\gtrsim 0.1$) that are lower than previous ones, for state numbers 15 and 72, respectively. These two eigenstates are not topological edge states, while they are actually bulk states with large dipole moments for NPs near the boundary. These kinds of eigenstates are formed due to the aperiodicity of the lattice (for periodic chains, there are no such bulk states since all bulk states are extended Bloch states). Except for these large values, the results of other bulk eigenstates are negligibly small. In Fig. 9(b), it can be clearly observed that in the commensurate lattice of $\beta = \frac{1}{4}$, topological edge states, with state numbers 25, 26, 75, and 76, can result in very large results, while the contributions of all bulk eigenstates are vanishingly small. Therefore, we can claim that topological edge states can indeed lead to much larger values of $|\sum_m V_{k,m} G_{0,xx}^{m1}|^2$ than bulk states in both incommensurate and commensurate lattices, as expected.

In the meanwhile, from Eq. (23), we can also explain the role of the damping coefficient γ. The most evident fact is $\mathcal{T}_{N,1}(\omega) \propto \chi_N(\omega)\chi_1(\omega)$, meaning a smaller γ would enhance $\chi_j(\omega)$ near the single-particle resonance frequency $\omega_{\mathrm{res}} =$
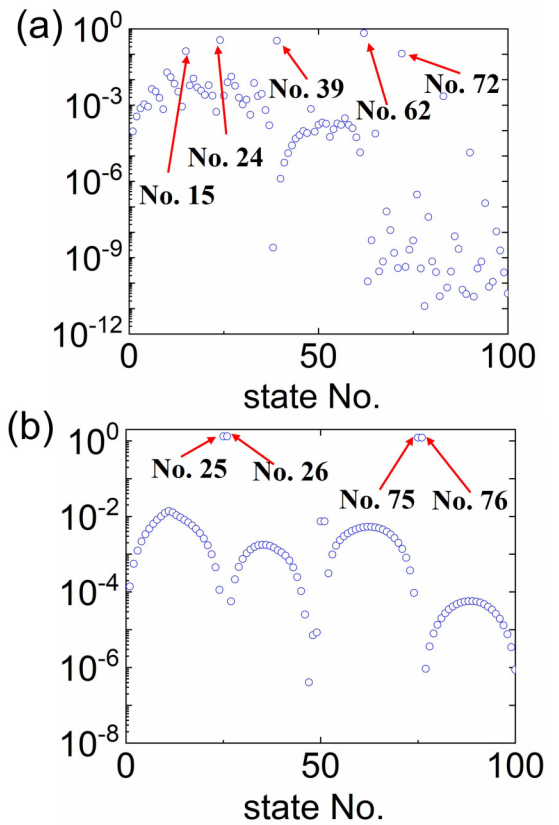

FIG. 9. Calculated results of $|\sum_m V_{k,m} G_{0,xx}^{m1}|^2$ for different eigenstates k in logarithmic scale for (a) the incommensurate case $\beta = (\sqrt{5} - 1)/2$ and (b) the commensurate case $\beta = \frac{1}{4}$. In both cases, the modulation phase is chosen to be $\phi = \pi$ in order to observe topological edge states. Other parameters are $N = 100$, $d = 0.6$ μm, and $\eta = 0.3$.

$\sqrt{(\varepsilon_\infty \omega_L^2 + 2\omega_T^2)/(\varepsilon_\infty + 2)} = 928.5$ cm^{-1} (see Appendix E) while reducing their off-resonance values. In particular, on resonance, $\chi_j(\omega_{\mathrm{res}}) \propto \gamma^{-1}$ [cf. Eqs. (3) and (E2) by neglecting the radiative correction]. This means if other factors fixed, the peak TC would be enhanced to be 25 times when γ is reduced from 5 to 1 cm^{-1}, while the observed enhancement of peak spectral heat rate is around 10. As aforementioned, it should also be noted that as γ decreases, the number of contributing eigenstates to the TC at a specific frequency would also decrease. To get more insights, let us investigate the prefactor $|1/[1 - \alpha(\omega)\lambda_k]|^2$ at the single-particle resonance frequency ($\omega = \omega_{\mathrm{res}}$) in Eq. (23) for each eigenstate k of the commensurate lattice $\beta = \frac{1}{4}$ at different damping coefficients as shown in Fig. 10.

In Fig. 10(a) for the $\phi = \pi$ case, we can see when $\gamma = 5$ cm^{-1}, not only those eigenstates very close to ω_{res} have relatively large prefactors [state numbers ranging from 27 to 74, residing in the middle two bands as given in Figs. 6(a)–6(c)] and thus main contributions to the TC, but also the eigenstates in the lowest and highest bands [state numbers ranging from 1 to 24 and from 77 to 100, cf. Figs. 6(a)–6(c)] show substantial prefactors due to the relatively large γ. The four points corresponding to topological edge states [state numbers are 25, 26, 75, and 76] can be clearly identified, which are isolated with
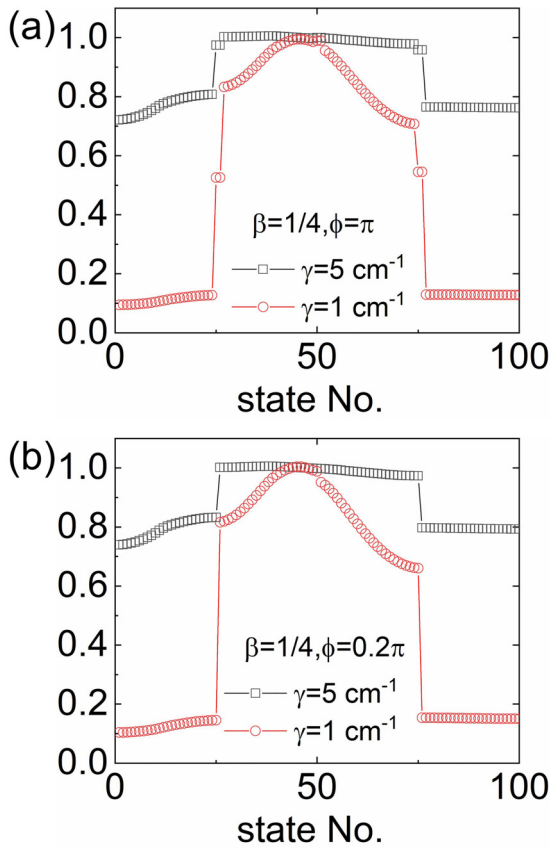
FIG. 10. Calculated results of the prefactor $|1/[1 - \alpha(\omega_{res})\lambda_k]|^2$ for different eigenstates k for the commensurate lattice $\beta = \frac{1}{4}$ when (a) $\phi = \pi$ and (b) $\phi = 0.2\pi$. Other parameters are $N = 100$, $d = 0.6$ μm, and $\eta = 0.3$.

those of other bulk states, with intermediate prefactors. On the other hand, when γ is reduced to 1 cm^{-1}, the prefactors for eigenstates in the lowest and highest bands significantly decrease to about 0.1 while the prefactors of eigenstates close to ω_{res} remain relatively large (yet they are also reduced in some degree). For the topological edge states, their prefactors are also reduced but are still larger than 0.5. As a comparison, Fig. 10(b) shows the case of $\phi = 0.2\pi$, in which no topological edge states are seen. It is thus evident that by reducing γ, the proportion contributed by the topological edge states to the TC increases [cf. Eq. (23)], and thus the contrast between topologically nontrivial and trivial cases becomes more substantial (cf. Figs. 7 and 8).

For completeness, more detailed discussions are presented in the Appendixes. In Appendix B, temperature profile and total radiative heat transfer rate under the thermal equilibrium scenario are investigated. In Appendix C, a comparison of our results with those of a regular periodic chain, that is, the monoatomic chain, is presented to further reveal the import role played by TPhPs. In Appendix D, we study the effect of a larger modulation amplitude η.

VI. CONCLUSIONS

To summarize, we show TPhPs can be realized in 1D bichromatic SiC nanoparticle chains and they can consid-

erably enhance radiative heat transfer for an array much longer than the wavelength of radiation. The introduction of incommensurate or commensurate modulations on the interparticle distances of 1D periodic chains leads to a mimicry of the off-diagonal AAH model. The eigenstate spectrum with respect to the modulation phase is calculated, which clearly demonstrates that under this type of modulation the chain supports nontrivial topological modes localized over the boundaries. This is because the present system inherits the topological property of two-dimensional IQH systems despite the presence of long-range dipole-dipole interactions. In this circumstance the gap-labeling theorem and corresponding Chern number can still be used to characterize the features of band gaps and topological edge modes. An exception is for the $\beta = \frac{1}{2}$ case whose topological property can be characterized by a Z_2 topological index in the Majorana basis. Moreover, based on many-body radiative heat transfer theory for a set of dipoles, we show the presence of topological gaps and midgap TPhPs can considerably enhance radiative heat transfer for an array much longer than the wavelength of radiation. We show how the modulation phase that acts as the synthetic dimension can tailor the radiative heat transfer rate by inducing or annihilating topological modes. We also find if the damping rate of the SiC material can be reduced, the enhancement of radiative heat transfer due to TPhPs can be significantly larger. Our theoretical analysis based on eigenvalue decomposition reveals the role of TPhPs quantitatively, whose localization behavior over the chain boundaries is shown to be crucial to the enhancement. These findings therefore provide a fascinating route for tailoring near-field radiative heat transfer based on the concept of topological physics.

We note in Refs. [95,96] a tight bound for radiative heat transfer between two bodies was derived, based on the so-called radiative efficacies obtained from the singular value decomposition (SVD) of off-diagonal vacuum Maxwell Green's function. These works, although developed for two-body problem, laid the foundation for estimating the radiative heat transfer limit for many-body system. In particular, when the radiative heat transfer between two specific bodies in an N-body system is considered, this method can be applied via replacing the vacuum GF in the two-body problem by the effective GF of the environment [note it would be different from $\mathbf{G}^{ij}$ in Eq. (13)] which accounts for the multiple scattering and many-body effects of the other $N - 2$ bodies. This method provides another route to establish the connection between topological edge states and radiative heat transfer and, more importantly, may be helpful for evaluating the fundamental limit of enhancement that topological edge states can bring.

As the concept of synthetic dimension due to the interparticle distance modulation can be further extended to create high-order topological systems such as four-dimensional (4D) high-order topological insulator and 4D Chern insulator [97], we expect more physical insights can be obtained if this concept is introduced to the many-particle system. Moreover, although the present system does not exhibit significant non-Hermiticity for the topological band that may alter the topological properties qualitatively, we envision that the presence of strong non-Hermiticity would have qualitative effects on the topological optical modes mediated radiative heat transfer [98–100]. Additional artificial non-Hermiticity can

be introduced, for instance, by adding appropriate gains into the system [101]. In this scenario, one may mimic the non-Hermitian $\mathcal{PT}$-symmetric AAH model [99,102,103], in which more interesting topological phenomena and radiative heat transfer properties may be observed. Magnetic field can also be introduced into the system to induce nonreciprocal hoppings, which can also result in a non-Hermitian Hamiltonian [104,105].

APPENDIX A: GAP-LABELING THEOREM

In this Appendix, we give a basic introduction to the gap-labeling theorem [Eq. (17)], which is well established and extensively discussed in many previous works. In 1982, Thouless, Kohmoto, Nightingale, and den Nijs (TKNN) [64] considered particular models of Bloch electrons in "rational" magnetic fields with flux $\varphi = \varphi_0 p/q$ per unit cell, where φ_0 is the quantum of magnetic flux and p, q are coprime integers. It was shown that a magnetic band b, which derives from the magnetic translational symmetry, can be characterized by an integer denoted by ν_b. This integer then determines the contribution of the band to the quantized Hall conductance of the system as $\nu_b e^2/h$ in linear-response theory, where e is the elementary charge and $h = 2\pi\hbar$ is the Planck's constant, respectively. This integer is a Chern topological invariant for the band [106,107] and satisfies the following Diophantine equation [64–66,69]:

$$p\nu_b + q\mu_b = 1. \tag{A1}$$

This equation thus constitutes the topological description of the integer quantum Hall effect (IQHE) in a 2D periodic potential. Then, by summing this equation over n magnetic bands, we have

$$\bar{\beta}\nu + \mu = \bar{\mathcal{N}} \tag{A2}$$

with $\bar{\beta} = p/q$ and $\bar{\mathcal{N}} = n/q$ for the gap between nth and $(n+1)$th magnetic bands [66]. In this sense, Eq. (17) in the main text can be regarded as the limiting case of the above equation by taking $p \to \infty$ and $q \to \infty$, to make $\bar{\beta} \to \beta$ become an irrational number, and the $\bar{\mathcal{N}}$ approaches $\mathcal{N}$ as the IDOS, since in this irrational case a magnetic band reduces to an infinitely degenerate level as a result of Cantor set feature of the spectrum [69]. In other words, the spectrum is a Cantor set with Lebesgue measure zero [59–61]. In such a 2D IQH system, $\nu e^2/h$ is the quantum Hall conductance of the system [66,108,109] and μe is the charge per unit cell that is transported when the periodic potential is dragged adiabatically by one lattice constant [108,109].

As a matter of fact, the gap-labeling theorem enables the topological classification of these gaps and plays for quasiperiodic systems a similar role to that of Bloch theorem for periodic ones [73,75,85]. More precisely, Bloch theorem labels the eigenstates of a periodic system with a quasimomentum and identifies topological invariants (Chern numbers) expressed in terms of a Berry curvature. This labeling is robust as long as the lattice translational symmetry is preserved. Similarly, the gap-labeling theorem permits to associate integer-valued topological invariants to each gap, which are K-theory invariants. Note they are not strictly speaking Chern numbers which describe the topology of smooth Riemannian manifolds. This is because quasiperiodic systems cannot be ascribed to such a smooth manifold. Nevertheless, there may exist an interpolation between both situations that could establish a link between Chern numbers and the above topological numbers appearing in the gap-labeling theorem [30]. As proved by Bellissard and coworkers [73,75,110], these integers can be given both a topological meaning and invariance properties akin in nature to Chern numbers but not expressible in terms of a curvature, unlike those in periodic system [cf. Eq. (18)].

APPENDIX B: EQUILIBRIUM TEMPERATURE FIELD AND HEAT TRANSFER RATE

In the main text, we are only concerned with the heat transfer rate between two nanoparticles at the opposite ends of the chain, although in the calculation we take all many-body dipole-dipole interactions and multiple scattering effects into account in the presence of other nanoparticles. The chain is out of thermal equilibrium. In this Appendix, we proceed to the calculation of equilibrium temperature field when the two end nanoparticles are at fixed temperatures, with $T_1 = 310$ K and $T_N = 300$ K, maintained by external thermal baths, and then compare the equilibrium radiative heat transfer rate as well as temperature distribution for topologically trivial and nontrivial chains.

Under thermal equilibrium, except for the particles at the two ends, the net power absorbed by each particle in the chain is equal to zero [111–114]:

$$\sum_{j=1, j\neq i}^{N} \mathcal{P}_{j\to i}(T_j) - \mathcal{P}_{i\to j}(T_i) = 0, \quad i = 2, \dots, N-1. \tag{B1}$$

Inserting Eq. (15) into above equation yields

$$\sum_{j=1, j\neq i}^{N} 3 \int_0^\infty \frac{d\omega}{2\pi} [\Theta(\omega, T_j)\mathcal{T}_{i,j}(\omega) - \Theta(\omega, T_i)\mathcal{T}_{j,i}(\omega)] = 0,$$
$$i = 2, \dots, N-1 \tag{B2}$$

which is a highly nonlinear equation due to the temperature dependence of the Planck oscillator. For convenience, we can assume the deviation of the temperature of any particle from some equilibrium state $[T_{eq}, \dots, T_{eq}]$ is quite small. For simplicity, here we assume $T_{eq} = 300$ K. Then, by introducing the

thermal conductance from particle j to particle i as [115,116]

$$
\begin{aligned}
\mathcal{G}_{ij}(T_j) &= \frac{\partial \mathcal{P}_{j\to i}}{\partial T_j} = 3 \int_0^\infty \frac{d\omega}{2\pi} \hbar\omega \frac{\partial f_{\mathrm{BE}}(\omega, T_j)}{\partial T_j} \mathcal{T}_{i,j}(\omega) \\
&= \int_0^\infty \frac{4\omega^4 \chi_i \chi_j}{c^4} \hbar\omega \frac{\partial f_{\mathrm{BE}}(\omega, T_j)}{\partial T_j} \mathrm{Tr}[\mathbf{G}^{ij}\mathbf{G}^{ij\dagger}] \frac{d\omega}{2\pi},
\end{aligned}
\tag{B3}
$$

we can linearize Eq. (B2),

$$
\sum_{j=1, j\neq i}^N \mathcal{G}_{ij}(T_{\mathrm{eq}})T_j - \mathcal{G}_{ji}(T_{\mathrm{eq}})T_i = 0, \quad i = 2, \ldots, N-1
\tag{B4}
$$

in which we assume $T_j = T_{\mathrm{eq}} + \Delta T_j$ and $T_i = T_{\mathrm{eq}} + \Delta T_i$ with $\Delta T_j \ll T_{\mathrm{eq}}$ and $\Delta T_i \ll T_{\mathrm{eq}}$, and the relation $\mathcal{G}_{ji}(T_{\mathrm{eq}}) = \mathcal{G}_{ij}(T_{\mathrm{eq}})$ due to reciprocity is applied. As a consequence, we get a set of $(N-2)$ equations for T_i, $i = 2, \ldots, N-1$. In a matrix notation, these equations can be written as the thermal equilibrium temperatures $\mathbf{T} = [T_2, \ldots, T_{N-1}]^{\mathrm{T}}$ can be written as

$$
\mathbf{T} = \mathbf{H}^{-1}\mathbf{b},
\tag{B5}
$$

where the matrix elements are given by

$$
H_{i-1,j-1} = \sum_{k=1, k\neq i}^N \mathcal{G}_{ki}\delta_{ij} - \mathcal{G}_{ij}(1 - \delta_{ij}), \quad i, j \neq 1, N
\tag{B6}
$$

and the column vector is given by

$$
\mathbf{b} = [(\mathcal{G}_{21}T_1 + \mathcal{G}_{2N}T_N), \ldots, (\mathcal{G}_{N-1,1}T_1 + \mathcal{G}_{N-1,N}T_N)]^{\mathrm{T}}.
\tag{B7}
$$

With the aid of equilibrium temperature field, we can obtain the total heat transfer rate through the chain by simply evaluating the total heat absorbed by particle N as [115,117]

$$
Q \approx \sum_{j=1}^{N-1} \mathcal{G}_{N,j}(T_{\mathrm{eq}})(T_j - T_N).
\tag{B8}
$$

The results of temperature distributions for the incommensurate lattice $\beta = (\sqrt{5} - 1)/2$ and commensurate lattice $\beta = \frac{1}{4}$ are shown in Figs. 11(a) and 11(c), for different modulation phases $\phi = 0.2\pi$ and π. No qualitative differences led by the presence of topological edge states in the $\phi = \pi$ scenarios are observed. Results for total radiative heat flux are also presented in Figs. 11(b) and 11(d) for the incommensurate lattice $\beta = (\sqrt{5} - 1)/2$ and commensurate lattice $\beta = \frac{1}{4}$, respectively, as a function of ϕ. Note we also plot the low-loss results in these figures. We can see the differences are quite small between topologically nontrivial and trivial cases. In a word, the equilibrium temperature field and total radiative heat transfer rate do not exhibit a similar ϕ dependence as $\mathcal{P}_{\mathrm{net}}^{N1}$ does. This is expected, as $\mathcal{P}_{\mathrm{net}}^{N1}$ ($\sim 10^{-19}$ W) is orders of magnitude smaller the total heat rate ($\sim 10^{-15}$ W), and thus the enhancement of heat transfer between the first and Nth NPs due to topological edge states has very small impacts on the total heat transfer processes in the entire chain.

Nevertheless, we emphasize that these results for thermally equilibrium systems do not mean our study is not relevant. Our study may still provide a method to mediate an enhancement
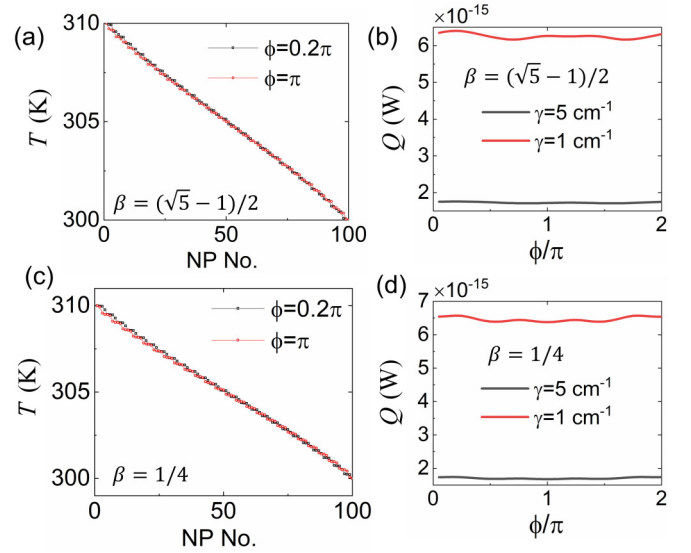

FIG. 11. Equilibrium temperature distribution and heat rate. (a) Temperatures of NPs in the $\beta = (\sqrt{5} - 1)/2$ chain for $\phi = 0.2\pi$ and π. (b) Radiative heat rate through the entire chain as a function of ϕ for different damping coefficients for the $\beta = (\sqrt{5} - 1)/2$ case. (c) Temperatures of NPs in the $\beta = \frac{1}{4}$ chain for $\phi = 0.2\pi$ and π. (d) Radiative heat rate through the entire chain as a function of ϕ for different damping coefficients for the $\beta = \frac{1}{4}$ case.

and modulation of heat transfer rate between two distant nano-objects, in which other particles in the chain, maintained at the same temperature with the low-temperature nano-object at the end, are used as enabling nanostructures. This may find applications, for instance, in thermal radiative circuits for manipulating and transmitting signals [28,118].

APPENDIX C: COMPARISON WITH PERIODIC MONOATOMIC CHAINS

It is instructive to compare the results in the main text with a regular periodic chain, that is, the monoatomic chain. We calculate the band structure of 1D monoatomic chains by choosing $\beta = 1$ in Eq. (1) with a period of $d[1 + \eta \cos(\phi)]$. By this way, we can study the dependence of radiative heat transfer rate as a function of ϕ. As expected, from the eigenstate spectrum shown in Fig. 12(a), no band gap exists in this simple chain, where all eigenstates demonstrate very small IPR values, indicating they are extended (Bloch) states.

The net spectral heat rate from the first NP to the last NP, $P_{\mathrm{net}}^{N1}(\omega)$ for $\phi = 0.5\pi$ and π, is plotted in Fig. 12(b). It is seen the latter case ($\phi = \pi$) shows a much larger spectral heat rate than the former case ($\phi = 0.5\pi$). It is also substantially larger than those in previous cases with topological edge states [cf. Figs. 3(a), 5(a), and 7(a)]. However, it is soon noted that this direct comparison is unfair as P_{net}^{N1} decays with the length of the chain in power law (L^{-2} or even faster where L is the length of the chain) due to dipole-dipole interactions [19]. When $\phi = \pi$, the period of the regular array is $0.7d$ and total length of the chain is much shorter than other chains. Actually, the lengths of the chains studied in the main text are always around $(N-1)d$, with very small variations (within 1%), corresponding to $\phi = 0.5\pi$ in the regular array.
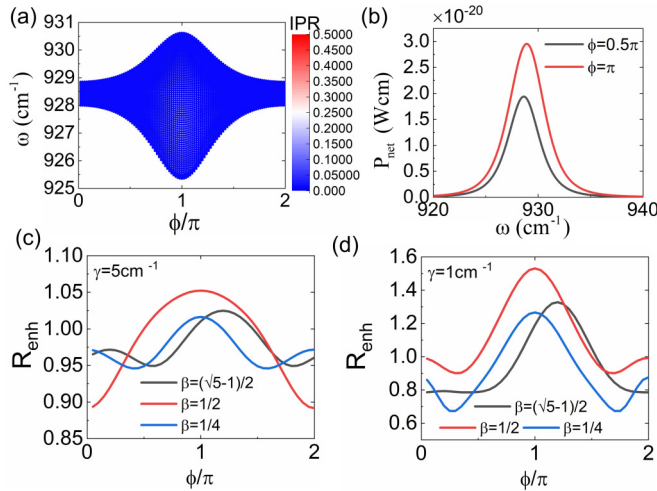
FIG. 12. Comparison with regular periodic arrays with $\beta = 1$, $N = 100$, $d = 0.6$ μm, and $\eta = 0.3$. (a) Longitudinal band structures. (b) Spectral net heat rate for $\phi = 0.5\pi$ and π and π. (c), (d) Total net radiative heat rate through the entire chain as a function of ϕ for (c) $\gamma = 5$ cm^{-1} and (d) $\gamma = 1$ cm^{-1}.

For a fair comparison, we control the period of the regular chain and define an enhancement ratio of $R_{\mathrm{enh}} = P_{\mathrm{net}}^{N1}(L)/P_{\mathrm{net,reg}}^{N1}(L)$ for any chain investigated in the main text by dividing its heat transfer rate by that of a regular periodic chain of the same length $P_{\mathrm{net,reg}}^{N1}(L)$. The results are shown in Fig. 12(c), and those in the low-loss scenario are given in Fig. 12(d), which evidence the presence of topological edge states can lead to an enhancement to radiative heat transfer.

APPENDIX D: EFFECT OF A LARGER η

We further investigate the situation with a large modulation amplitude $\eta = 0.5$. By Eq. (1), the smallest interparticle distance is $d(1 - \eta) = 0.5d > 3a$, and thus dipole approximation suffices to demonstrate the many-particle physics. Figure 13(a) shows the longitudinal band structure for the incommensurate lattice [$\beta = (\sqrt{5} - 1)/2$]. Due to the increase of modulation amplitude, the band gaps widen substantially, and the IPRs of eigenstates within the bulk bands grow substantially compared to the $\eta = 0.3$ case. It can been seen the majority of bulk states in the spectrum are localized states with IPR values near or higher than 0.5. This phenomenon is a consequence of localization transition, a similar behavior to the conventional off-diagonal AAH model at large modulations [32,63]. Note this transition is a peculiar phenomenon in 1D quasiperiodic AAH model [32,63]. The topological edge states with IPR values around 0.5, emerging at the two main gaps, can be observed in this case, as expected. This indicates the variation of modulation amplitude does not affect the topological property of the chain. The calculated results of total net radiative heat transfer rate for $\gamma = 5$ and 1 cm^{-1} are presented in Fig. 13(b), clearly demonstrating the enhancement brought by these topological edge states, especially for the low-loss scenario, as expected.

We then consider the commensurate lattice with $\beta = \frac{1}{4}$. Due to the large modulations, the band gaps also get wider compared to the $\eta = 0.3$ scenario, due to stronger
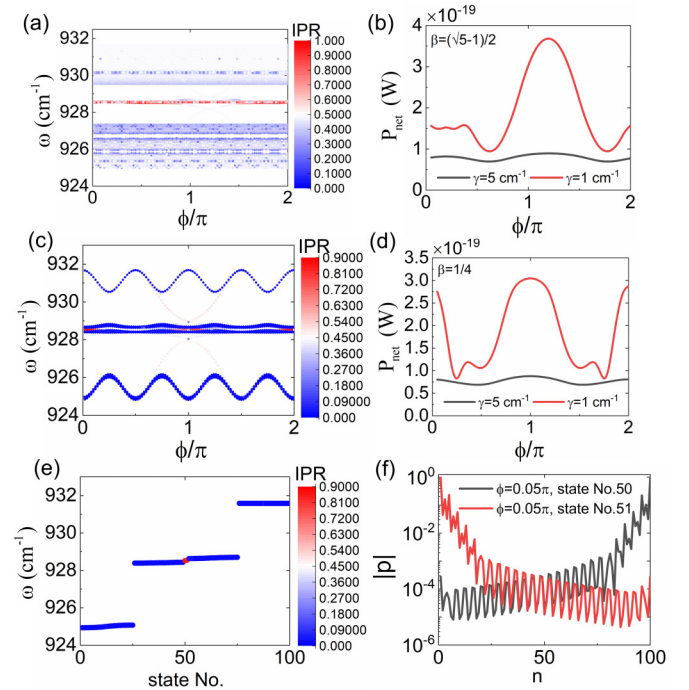

FIG. 13. AAH chains with $\eta = 0.5$. (a) Longitudinal band structure for $\beta = (\sqrt{5} - 1)/2$. Note there are topological edge states with IPRs around 0.5 in the two main gaps denoted by very light colors. (b) Total net radiative heat rate for $\beta = (\sqrt{5} - 1)/2$ as a function of ϕ under different damping coefficients. (c) Longitudinal band structure for $\beta = \frac{1}{4}$. Note there are topological edge states with IPRs around 0.5 in the two main gaps denoted by very light colors. (d) Total net radiative heat rate for $\beta = \frac{1}{4}$ as a function of ϕ under different damping coefficients. (e) Eigenstate spectrum for $\beta = \frac{1}{4}$ and $\phi = 0.05\pi$. (f) Dipole moment distributions for the midgap states (state numbers 50 and 51) in the small gap separating the central two bands for $\phi = 0.05\pi$.

dipole-dipole interactions in the near field arising from the reduced interparticle distance. Another feature is that, for a specific ϕ, the eigenstates in each band are concentrated in a smaller range of eigenfrequencies [cf. Fig. 13(e) for the case
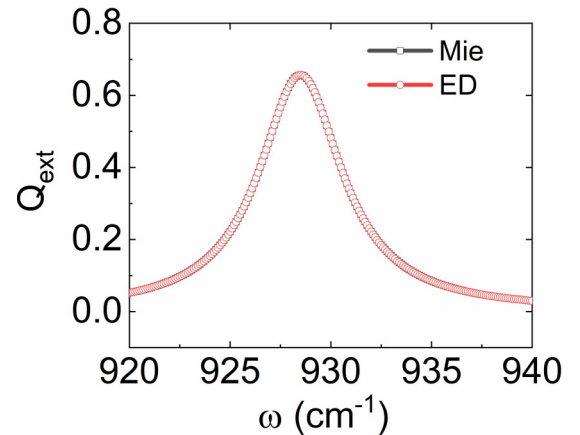

FIG. 14. Extinction efficiency Q_{ext} of a single SiC NP with a radius of $a = 0.1$ μm calculated from the Mie theory, compared with the result under the electric dipole (ED) approximation.

of $\phi = 0.05\pi$]. The topological edge states traversing the two main gaps, or TPhPs, can still be observed. We can calculate the total net radiative heat rate $P_{\text{net,max}}^{N1}$ as a function of ϕ for $\gamma = 5$ and 1 cm^{-1}, given in Fig. 13(d). The "high-loss" curve is very similar to that in the $\eta = 0.3$ [cf. Fig. 7(b)], while the "low-loss" one shows a distinct line shape from that in $\eta = 0.3$ [cf. Fig. 8(b)], in which $P_{\text{net,max}}^{N1}$ exhibits large values at small ϕ's. This arises from the contribution of the topological edge states (state numbers 50 and 51) in the central band gap formed between the central two bands [cf. Fig. 13(e) for the eigenstate spectrum of $\phi = 0.05\pi$]. These topological edge modes are protected by larger Chern values $\nu = 2$ [34,119]. The dipole moment distributes these states, evidencing the localization behavior near the chain boundaries [Fig. 13(f)].

APPENDIX E: COMPARISON BETWEEN ELECTRIC DIPOLE APPROXIMATION AND MIE THEORY

To validate the electric dipole approximation of polarizability for SiC NPs. we compare the results of single-particle extinction efficiency $Q_{\text{ext}} = C_{\text{ext}}/(\pi a^2)$ calculated by the Mie theory and the ED approximation, where C_{ext} is the extinction cross section, shown in Fig. 14. A good agreement is observed.

Here we also give the expression for the single-particle resonance frequency ω_{res}. Inserting the expression of ε_p, Eq. (2), into the Eq. (4) yields

$$\alpha_0(\omega) = \frac{\left(\varepsilon_\infty \omega_L^2 - \omega_T^2\right) - (\varepsilon_\infty - 1)\omega^2 - i(\varepsilon_\infty - 1)\omega\gamma}{\left(\varepsilon_\infty \omega_L^2 + 2\omega_T^2\right) - (\varepsilon_\infty + 2)\omega^2 - (\varepsilon_\infty + 2)i\omega\gamma}.$$
(E1)

Letting $\omega_{\text{res}} = \sqrt{\frac{\varepsilon_\infty \omega_L^2 + 2\omega_T^2}{(\varepsilon_\infty + 2)}} = 928.5$ cm^{-1} and $\omega'_{\text{res}} = \sqrt{\frac{\varepsilon_\infty \omega_L^2 - \omega_T^2}{(\varepsilon_\infty - 1)}} = 993.7$ cm^{-1}, we have

$$\alpha_0(\omega) = \frac{\varepsilon_\infty - 1}{\varepsilon_\infty + 2} \frac{\omega'^2_{\text{res}} - \omega^2 - i\omega\gamma}{\omega_{\text{res}}^2 - \omega^2 - i\omega\gamma}.$$
(E2)

As radiative correction in Eq. (3) is quite small for the radius under investigation, the single-particle resonance frequency lies approximately at $\omega = \omega_{\text{res}}$, which also agrees well with Mie theory calculation.

[1] J. Xiao and B. Yan, First-principles calculations for topological quantum materials, Nat. Rev. Phys. **3**, 283 (2021).

[2] T. Ozawa, H. M. Price, A. Amo, N. Goldman, M. Hafezi, L. Lu, M. C. Rechtsman, D. Schuster, J. Simon, O. Zilberberg, and I. Carusotto, Topological photonics, Rev. Mod. Phys. **91**, 015006 (2019).

[3] M. Atala, M. Aidelsburger, J. T. Barreiro, D. Abanin, T. Kitagawa, E. Demler, and I. Bloch, Direct measurement of the zak phase in topological bloch bands, Nat. Phys. **9**, 795 (2013).

[4] C. He, X. Ni, H. Ge, X.-C. Sun, Y.-B. Chen, M.-H. Lu, X.-P. Liu, and Y.-F. Chen, Acoustic topological insulator and robust one-way sound transport, Nat. Phys. **12**, 1124 (2016).

[5] R. Süsstrunk and S. D. Huber, Observation of phononic helical edge states in a mechanical topological insulator, Science **349**, 47 (2015).

[6] M. Z. Hasan and C. L. Kane, Colloquium: Topological insulators, Rev. Mod. Phys. **82**, 3045 (2010).

[7] A. B. Khanikaev, S. H. Mousavi, W.-K. Tse, M. Kargarian, A. H. MacDonald, and G. Shvets, Photonic topological insulators, Nat. Mater. **12**, 233 (2013).

[8] L. Lu, J. D. Joannopoulos, and M. Soljačić, Topological photonics, Nat. Photonics **8**, 821 (2014).

[9] A. B. Khanikaev and G. Shvets, Two-dimensional topological photonics, Nat. Photonics **11**, 763 (2017).

[10] M. Li, D. Zhirihin, M. Gorlach, X. Ni, D. Filonov, A. Slobozhanyuk, A. Alù, and A. B. Khanikaev, Higher-order topological states in photonic kagome crystals with long-range interactions, Nat. Photonics **14**, 89 (2020).

[11] H. Zhao, X. Qiao, T. Wu, B. Midya, S. Longhi, and L. Feng, Non-hermitian topological light steering, Science **365**, 1163 (2019).

[12] C. Poli, M. Bellec, U. Kuhl, F. Mortessagne, and H. Schomerus, Selective enhancement of topologically induced interface states in a dielectric resonator chain, Nat. Commun. **6**, 6710 (2015).

[13] R. El-Ganainy and M. Levy, Optical isolation in topological-edge-state photonic arrays, Opt. Lett. **40**, 5275 (2015).

[14] D. Karki, R. El-Ganainy, and M. Levy, Toward High-Performing Topological Edge-State Optical Isolators, Phys. Rev. Appl. **11**, 034045 (2019).

[15] M. Parto, S. Wittek, H. Hodaei, G. Harari, M. A. Bandres, J. Ren, M. C. Rechtsman, M. Segev, D. N. Christodoulides, and M. Khajavikhan, Edge-Mode Lasing in 1D Topological Active Arrays, Phys. Rev. Lett. **120**, 113901 (2018).

[16] Y. Zeng, U. Chattopadhyay, B. Zhu, B. Qiang, J. Li, Y. Jin, L. Li, A. G. Davies, E. H. Linfield, B. Zhang et al., Electrically pumped topological laser with valley edge modes, Nature (London) **578**, 246 (2020).

[17] Z.-K. Shao, H.-Z. Chen, S. Wang, X.-R. Mao, Z.-Q. Yang, S.-L. Wang, X.-X. Wang, X. Hu, and R.-M. Ma, A high-performance topological bulk laser based on band-inversion-induced reflection, Nat. Nanotechnol. **15**, 67 (2020).

[18] B. X. Wang and C. Y. Zhao, Terahertz topological plasmon polaritons for robust temperature sensing, Phys. Rev. Mater. **4**, 075201 (2020).

[19] A. Ott and S.-A. Biehs, Radiative heat flux through a topological su-schrieffer-heeger chain of plasmonic nanoparticles, Phys. Rev. B **102**, 115417 (2020).

[20] A. Ott, Z. An, A. Kittel, and S.-A. Biehs, Thermal near-field energy density and local density of states in topological one-dimensional su-schrieffer-heeger chains and two-dimensional su-schrieffer-heeger lattices of plasmonic nanoparticles, Phys. Rev. B **104**, 165407 (2021).

[21] A. Ott and S.-A. Biehs, Topological near-field heat flow in a honeycomb lattice, Int. J. Heat Mass Transfer **190**, 122796 (2022).

[22] B. X. Wang and C. Y. Zhao, Topological phonon polaritons in one-dimensional non-hermitian silicon carbide nanoparticle chains, Phys. Rev. B **98**, 165435 (2018).

[23] B. X. Wang and C. Y. Zhao, Wideband tunable infrared topological plasmon polaritons in dimerized chains of doped-silicon nanoparticles, J. Appl. Phys. **127**, 073106 (2020).

[24] P. Ben-Abdallah, S.-A. Biehs, and K. Joulain, Many-Body Radiative Heat Transfer Theory, Phys. Rev. Lett. **107**, 114301 (2011).

[25] J. Dong, J. Zhao, and L. Liu, Radiative heat transfer in many-body systems: Coupled electric and magnetic dipole approach, Phys. Rev. B **95**, 125411 (2017).

[26] J. Chen, C. Zhao, and B. Wang, Near-field thermal radiative transfer in assembled spherical systems composed of core-shell nanoparticles, J. Quant. Spectrosc. Radiat. Transfer **219**, 304 (2018).

[27] J.-L. Fang, L. Qu, Y. Zhang, and H.-L. Yi, Resonant radiative heat transfer and many-body effects between nanoparticles and a multilayered slab, Phys. Rev. B **102**, 245418 (2020).

[28] S.-A. Biehs, R. Messina, P. S. Venkataram, A. W. Rodriguez, J. C. Cuevas, and P. Ben-Abdallah, Near-field radiative heat transfer in many-body systems, Rev. Mod. Phys. **93**, 025009 (2021).

[29] J. Song, Q. Cheng, B. Zhang, L. Lu, X. Zhou, Z. Luo, and R. Hu, Many-body near-field radiative heat transfer: methods, functionalities and applications, Rep. Prog. Phys. **84**, 036501 (2021).

[30] Y. E. Kraus and O. Zilberberg, Topological Equivalence between the Fibonacci Quasicrystal and the Harper Model, Phys. Rev. Lett. **109**, 116404 (2012).

[31] Y. E. Kraus, Y. Lahini, Z. Ringel, M. Verbin, and O. Zilberberg, Topological States and Adiabatic Pumping in Quasicrystals, Phys. Rev. Lett. **109**, 106402 (2012).

[32] S. Ganeshan, K. Sun, and S. Das Sarma, Topological Zero-Energy Modes in Gapless Commensurate Aubry-André-Harper Models, Phys. Rev. Lett. **110**, 180403 (2013).

[33] M. Verbin, O. Zilberberg, Y. E. Kraus, Y. Lahini, and Y. Silberberg, Observation of Topological Phase Transitions in Photonic Quasicrystals, Phys. Rev. Lett. **110**, 076403 (2013).

[34] A. V. Poshakinskiy, A. N. Poddubny, L. Pilozzi, and E. L. Ivchenko, Radiative Topological States in Resonant Photonic Crystals, Phys. Rev. Lett. **112**, 107403 (2014).

[35] F. Alpeggiani and L. Kuipers, Topological edge states in bichromatic photonic crystals, Optica **6**, 96 (2019).

[36] T. Chalopin, T. Satoor, A. Evrard, V. Makhalov, J. Dalibard, R. Lopes, and S. Nascimbene, Probing chiral edge dynamics and bulk topology of a synthetic hall system, Nat. Phys. **16**, 1017 (2020).

[37] P. Li, I. Dolado, F. J. Alfaro-Mozaz, F. Casanova, L. E. Hueso, S. Liu, J. H. Edgar, A. Y. Nikitin, S. Vélez, and R. Hillenbrand, Infrared hyperbolic metasurface based on nanostructured van der waals materials, Science **359**, 892 (2018).

[38] S. Foteinopoulou, G. C. R. Devarapu, G. S. Subramania, S. Krishna, and D. Wasserman, Phonon-polaritonics: Enabling powerful capabilities for infrared photonics, Nanophotonics **8**, 2129 (2019).

[39] A. I. Volokitin and B. N. J. Persson, Near-field radiative heat transfer and noncontact friction, Rev. Mod. Phys. **79**, 1291 (2007).

[40] B. Song, Y. Ganjeh, S. Sadat, D. Thompson, A. Fiorino, V. Fernández-Hurtado, J. Feist, F. J. Garcia-Vidal, J. C.

Cuevas, P. Reddy *et al.*, Enhancement of near-field radiative heat transfer using polar dielectric thin films, Nat. Nanotechnol. **10**, 253 (2015).

[41] J. Dong, J. Zhao, and L. Liu, Long-distance near-field energy transport via propagating surface waves, Phys. Rev. B **97**, 075422 (2018).

[42] J. Chen, B. Wang, and C. Zhao, Scattering-type multi-probe scanning thermal microscope based on near-field thermal radiation, Int. J. Heat Mass Transfer **181**, 121869 (2021).

[43] W. Zhang, B. Wang, and C. Zhao, Active control and enhancement of near-field heat transfer between dissimilar materials by strong coupling effects, Int. J. Heat Mass Transfer **188**, 122588 (2022).

[44] J.-L. Fang, L. Qu, Y. Zhang, and H.-L. Yi, High enhancement of near-field radiative heat transfer between nanoparticles via the surface modes of the dielectric thin film, Int. J. Heat Mass Transfer **190**, 122711 (2022).

[45] L. Pilozzi and C. Conti, Topological lasing in resonant photonic structures, Phys. Rev. B **93**, 195317 (2016).

[46] A. Jagannathan, The fibonacci quasicrystal: Case study of hidden dimensions and multifractality, Rev. Mod. Phys. **93**, 045001 (2021).

[47] M. S. Wheeler, J. S. Aitchison, J. I. L. Chen, G. A. Ozin, and M. Mojahedi, Infrared magnetic response in a random silicon carbide micropowder, Phys. Rev. B **79**, 073103 (2009).

[48] E. Tervo, Z. Zhang, and B. Cola, Collective near-field thermal emission from polaritonic nanoparticle arrays, Phys. Rev. Mater. **1**, 015201 (2017).

[49] V. A. Markel and A. K. Sarychev, Propagation of surface plasmons in ordered and disordered chains of metal nanospheres, Phys. Rev. B **75**, 085426 (2007).

[50] S. Y. Park and D. Stroud, Surface-plasmon dispersion relations in chains of metallic nanoparticles: An exact quasistatic calculation, Phys. Rev. B **69**, 125418 (2004).

[51] W. H. Weber and G. W. Ford, Propagation of optical excitations by dipolar interactions in metal nanoparticle chains, Phys. Rev. B **70**, 125429 (2004).

[52] S. Pocock, X. Xiao, P. A. Huidobro, and V. Giannini, The topological plasmonic chain with retardation and radiative effects, ACS Photonics **5**, 2271 (2018).

[53] H. Cao and J. Wiersig, Dielectric microcavities: Model systems for wave chaos and non-hermitian physics, Rev. Mod. Phys. **87**, 61 (2015).

[54] R. Wang, M. Röntgen, C. V. Morfonios, F. A. Pinheiro, P. Schmelcher, and L. D. Negro, Edge modes of scattering chains with aperiodic order, Opt. Lett. **43**, 1986 (2018).

[55] B. X. Wang and C. Y. Zhao, Topological photonic states in one-dimensional dimerized ultracold atomic chains, Phys. Rev. A **98**, 023808 (2018).

[56] B. X. Wang and C. Y. Zhao, Interferences and localization in disordered media with anisotropic structural correlations, J. Appl. Phys. **130**, 133101 (2021).

[57] B. X. Wang and C. Y. Zhao, Near-resonant light transmission in two-dimensional dense cold atomic media with short-range positional correlations, J. Opt. Soc. Am. B **37**, 1757 (2020).

[58] B. X. Wang and C. Y. Zhao, Topological quantum optical states in quasiperiodic cold atomic chains, Phys. Rev. A **103**, 013727 (2021).

[59] M. Kohmoto, Metal-Insulator Transition and Scaling for Incommensurate Systems, Phys. Rev. Lett. **51**, 1198 (1983).

[60] M. Kohmoto, B. Sutherland, and K. Iguchi, Localization of Optics: Quasiperiodic media, Phys. Rev. Lett. **58**, 2436 (1987).

[61] A. Avila and S. Jitomirskaya, The ten martini problem, Ann. Math. **170**, 303 (2009).

[62] S. Longhi, Metal-insulator phase transition in a non-hermitian aubry-andré-harper model, Phys. Rev. B **100**, 125157 (2019).

[63] Y. Lahini, R. Pugatch, F. Pozzi, M. Sorel, R. Morandotti, N. Davidson, and Y. Silberberg, Observation of a Localization Transition in Quasiperiodic Photonic Lattices, Phys. Rev. Lett. **103**, 013901 (2009).

[64] D. J. Thouless, M. Kohmoto, M. P. Nightingale, and M. den Nijs, Quantized Hall Conductance in a Two-Dimensional Periodic Potential, Phys. Rev. Lett. **49**, 405 (1982).

[65] A. H. MacDonald, Quantized hall effect in a hexagonal periodic potential, Phys. Rev. B **29**, 3057 (1984).

[66] I. Dana, Y. Avron, and J. Zak, Quantised hall conductance in a perfect crystal, J. Phys. C: Solid State Phys. **18**, L679 (1985).

[67] G. Amit and I. Dana, Topological phase transitions from harper to fibonacci crystals, Phys. Rev. B **97**, 075137 (2018).

[68] I. Dana and J. Zak, Quantum hall conductances and localization in a magnetic field, Phys. Rev. B **32**, 3612 (1985).

[69] I. Dana, Topologically universal spectral hierarchies of quasiperiodic systems, Phys. Rev. B **89**, 205111 (2014).

[70] T. Cookmeyer, J. Motruk, and J. E. Moore, Critical properties of the ground-state localization-delocalization transition in the many-particle aubry-andré model, Phys. Rev. B **101**, 174203 (2020).

[71] B. Simon, Almost periodic schrödinger operators: A review, Adv. Appl. Math. **3**, 463 (1982).

[72] J. M. Luck, Cantor spectra and scaling of gap widths in deterministic aperiodic systems, Phys. Rev. B **39**, 5834 (1989).

[73] J. Bellissard, A. Bovier, and J.-M. Ghez, Gap labelling theorems for one dimensional discrete schrödinger operators, Rev. Math. Phys. **04**, 1 (1992).

[74] Y. Hatsugai and M. Kohmoto, Energy spectrum and the quantum hall effect on the square lattice with next-nearest-neighbor hopping, Phys. Rev. B **42**, 8282 (1990).

[75] J. Bellissard, B. Iochum, E. Scoppola, and D. Testard, Spectral properties of one dimensional quasi-crystals, Commun. Math. Phys. **125**, 527 (1989).

[76] Y. Liu, X. Fu, W. Deng, and S. Wang, Gap-labeling properties of the energy spectrum for one-dimensional fibonacci quasilattices, Phys. Rev. B **46**, 9216 (1992).

[77] X. Fu, Y. Liu, P. Zhou, and W. Sritrakool, Perfect self-similarity of energy spectra and gap-labeling properties in one-dimensional fibonacci-class quasilattices, Phys. Rev. B **55**, 2882 (1997).

[78] F. Baboux, E. Levy, A. Lemaître, C. Gómez, E. Galopin, L. Le Gratiet, I. Sagnes, A. Amo, J. Bloch, and E. Akkermans, Measuring topological invariants from generalized edge states in polaritonic quasicrystals, Phys. Rev. B **95**, 161114(R) (2017).

[79] D. Tanese, E. Gurevich, F. Baboux, T. Jacqmin, A. Lemaître, E. Galopin, I. Sagnes, A. Amo, J. Bloch, and E. Akkermans, Fractal Energy Spectrum of a Polariton Gas in a Fibonacci Quasiperiodic Potential, Phys. Rev. Lett. **112**, 146404 (2014).

[80] N. X. A. Rivolta, H. Benisty, and B. Maes, Topological edge modes with $\mathcal{PT}$ symmetry in a quasiperiodic structure, Phys. Rev. A **96**, 023864 (2017).

[81] D. J. Apigo, K. Qian, C. Prodan, and E. Prodan, Topological edge modes by smart patterning, Phys. Rev. Mater. **2**, 124203 (2018).

[82] G. Rai, S. Haas, and A. Jagannathan, Proximity effect in a superconductor-quasicrystal hybrid ring, Phys. Rev. B **100**, 165121 (2019).

[83] D. J. Apigo, W. Cheng, K. F. Dobiszewski, E. Prodan, and C. Prodan, Observation of Topological Edge Modes in a Quasiperiodic Acoustic Waveguide, Phys. Rev. Lett. **122**, 095501 (2019).

[84] E. Levy, A. Barak, A. Fisher, and E. Akkermans, Topological properties of Fibonacci quasicrystals: A scattering analysis of Chern numbers, arXiv:1509.04028.

[85] A. Dareau, E. Levy, M. B. Aguilera, R. Bouganne, E. Akkermans, F. Gerbier, and J. Beugnon, Revealing the Topology of Quasicrystals with a Diffraction Experiment, Phys. Rev. Lett. **119**, 215304 (2017).

[86] D. Vodola, L. Lepori, E. Ercolessi, A. V. Gorshkov, and G. Pupillo, Kitaev Chains with Long-Range Pairing, Phys. Rev. Lett. **113**, 156402 (2014).

[87] O. Viyuela, D. Vodola, G. Pupillo, and M. A. Martin-Delgado, Topological massive dirac edge modes and long-range superconducting hamiltonians, Phys. Rev. B **94**, 125121 (2016).

[88] L. Lepori and L. Dell'Anna, Long-range topological insulators and weakened bulk-boundary correspondence, New J. Phys. **19**, 103030 (2017).

[89] Z. Guo, H. Jiang, Y. Sun, Y. Li, and H. Chen, Asymmetric topological edge states in a quasiperiodic harper chain composed of split-ring resonators, Opt. Lett. **43**, 5142 (2018).

[90] A. Lau, C. Ortix, and J. van den Brink, Topological Edge States with Zero Hall Conductivity in a Dimerized Hofstadter Model, Phys. Rev. Lett. **115**, 216805 (2015).

[91] L. Li, Z. Xu, and S. Chen, Topological phases of generalized su-schrieffer-heeger models, Phys. Rev. B **89**, 085111 (2014).

[92] J. Cao, Y. Xing, L. Qi, D.-Y. Wang, C.-H. Bai, A.-D. Zhu, S. Zhang, and H.-F. Wang, Simulating and studying the topological properties of generalized commensurate aubry–andré–harper model with microresonator array, Laser Phys. Lett. **15**, 015211 (2018).

[93] C. W. Ling, M. Xiao, C. T. Chan, S. F. Yu, and K. H. Fung, Topological edge plasmon modes between diatomic chains of plasmonic nanoparticles, Opt. Express **23**, 2021 (2015).

[94] C. Kathmann, R. Messina, P. Ben-Abdallah, and S.-A. Biehs, Limitations of kinetic theory to describe near-field heat exchanges in many-body systems, Phys. Rev. B **98**, 115434 (2018).

[95] P. S. Venkataram, S. Molesky, W. Jin, and A. W. Rodriguez, Fundamental Limits to Radiative Heat Transfer: The Limited Role of Nanostructuring in the Near-Field, Phys. Rev. Lett. **124**, 013904 (2020).

[96] S. Molesky, P. S. Venkataram, W. Jin, and A. W. Rodriguez, Fundamental limits to radiative heat transfer: Theory, Phys. Rev. B **101**, 035408 (2020).

[97] Z.-G. Chen, W. Zhu, Y. Tan, L. Wang, and G. Ma, Acoustic Realization of a Four-Dimensional Higher-Order Chern Insulator and Boundary-Modes Engineering, Phys. Rev. X **11**, 011016 (2021).

[98] S. Longhi, Topological Phase Transition in Non-Hermitian Quasicrystals, Phys. Rev. Lett. **122**, 237601 (2019).

[99] Q.-B. Zeng, Y.-B. Yang, and Y. Xu, Topological phases in non-hermitian aubry-andré-harper models, Phys. Rev. B **101**, 020201(R) (2020).

[100] X. Cai, Boundary-dependent self-dualities, winding numbers, and asymmetrical localization in non-hermitian aperiodic one-dimensional models, Phys. Rev. B **103**, 014201 (2021).

[101] M. A. K. Othman, V. Galdi, and F. Capolino, Exceptional points of degeneracy and $\mathcal{PT}$ symmetry in photonic coupled chains of scatterers, Phys. Rev. B **95**, 104305 (2017).

[102] Q.-B. Zeng and Y. Xu, Winding numbers and generalized mobility edges in non-hermitian systems, Phys. Rev. Res. **2**, 033052 (2020).

[103] A. P. Acharya, A. Chakrabarty, D. K. Sahu, and S. Datta, Localization, $\mathcal{PT}$ symmetry breaking, and topological transitions in non-hermitian quasicrystals, Phys. Rev. B **105**, 014202 (2022).

[104] E. J. Bergholtz, J. C. Budich, and F. K. Kunst, Exceptional topology of non-hermitian systems, Rev. Mod. Phys. **93**, 015005 (2021).

[105] S. Yao and Z. Wang, Edge States and Topological Invariants of Non-Hermitian Systems, Phys. Rev. Lett. **121**, 086803 (2018).

[106] J. E. Avron, R. Seiler, and B. Simon, Homotopy and Quantization in Condensed Matter Physics, Phys. Rev. Lett. **51**, 51 (1983).

[107] B. Simon, Holonomy, the Quantum Adiabatic Theorem, and Berry's Phase, Phys. Rev. Lett. **51**, 2167 (1983).

[108] H. Kunz, Quantized Currents and Topological Invariants for Electrons in Incommensurate Potentials, Phys. Rev. Lett. **57**, 1095 (1986).

[109] A. H. MacDonald, Landau-level subband structure of electrons on a square lattice, Phys. Rev. B **28**, 6713 (1983).

[110] J. Bellissard, Gap labelling theorems for Schrödinger operators, in *From Number Theory to Physics*, edited by M. Waldschmidt, P. Moussa, J.-M. Luck, and C. Itzykson (Springer, Berlin, 1992), pp. 538–630.

[111] L. Qu, Y. Zhang, J.-L. Fang, and H.-L. Yi, Steady-state temperature distribution under near-field radiative heat transfer inside a linear chain of polaritonic nanoparticles, J. Quant. Spectrosc. Radiat. Transfer **258**, 107404 (2021).

[112] P. Ben-Abdallah and A. W. Rodriguez, Controlling Local Thermal States in Classical Many-Body Systems, Phys. Rev. Lett. **129**, 260602 (2022).

[113] S. Sanders, L. Zundel, W. J. M. Kort-Kamp, D. A. R. Dalvit, and A. Manjavacas, Near-Field Radiative Heat Transfer Eigenmodes, Phys. Rev. Lett. **126**, 193601 (2021).

[114] P. Ben-Abdallah, Thermal photon drag in many-body systems, Phys. Rev. B **99**, 201406(R) (2019).

[115] E. J. Tervo, B. A. Cola, and Z. M. Zhang, Comparison of kinetic theory and fluctuational electrodynamics for radiative heat transfer in nanoparticle chains, J. Quant. Spectrosc. Radiat. Transfer **246**, 106947 (2020).

[116] P. Ben-Abdallah, K. Joulain, J. Drevillon, and C. Le Goff, Heat transport through plasmonic interactions in closely spaced metallic nanoparticle chains, Phys. Rev. B **77**, 075417 (2008).

[117] E. Tervo, M. Francoeur, B. Cola, and Z. Zhang, Thermal radiation in systems of many dipoles, Phys. Rev. B **100**, 205422 (2019).

[118] P. Ben-Abdallah and S.-A. Biehs, Near-Field Thermal Transistor, Phys. Rev. Lett. **112**, 044301 (2014).

[119] S. A. Skirlo, L. Lu, Y. Igarashi, Q. Yan, J. Joannopoulos, and M. Soljačić, Experimental Observation of Large Chern Numbers in Photonic Crystals, Phys. Rev. Lett. **115**, 253901 (2015).